Visa Suomi

3-D Motion-Tracking for High-Intensity Focused Ultrasound Therapy

School of Science

Thesis submitted for examination for the degree of Master of Science in Technology.

Espoo 7.8.2012

Thesis supervisor:

Prof. Esko Kauppinen

Thesis instructor:

M.Sc. (Tech.) Matti Tillander

Aalto University
School of Science

AALTO UNIVERSITY
SCHOOL OF SCIENCE

ABSTRACT OF THE
MASTER'S THESIS

Author: Visa Suomi

Title: 3-D Motion-Tracking for High-Intensity Focused Ultrasound Therapy

Date: 7.8.2012 Language: English Number of pages:9+52

Department of Applied Physics

Professorship: Engineering Physics Code: Tfy-3

Supervisor: Prof. Esko Kauppinen

Instructor: M.Sc. (Tech.) Matti Tillander

Respiratory motion during high-intensity focused ultrasound (HIFU) therapy reduces the efficiency of the treatment in abdominal organs. Hence, for the purpose of motion-correction during HIFU therapy, two different ultrasound-based 3-D motion-tracking methods were presented and adapted to the existing Philips Sonalleve MR-HIFU platform. The displacement estimation accuracies of these two techniques were determined using a metal pin and an *in vitro* tissue sample as targets. The measurement data was collected on all movement directions using element clusters consisting of one, three and 32 transmitting transducer elements. Simulations of the acoustic fields were also performed in order to discuss the theoretical limitations of the motion-tracking with the existing HIFU system.

The displacement estimation accuracies did not differ significantly for the two different techniques introduced but was rather dependent on the transmitting element cluster size and the orientation of the ultrasound beam axis. Using smaller number of elements and defining the beam axis angle accurately in the calculation algorithm yielded more stable results. The motion-tracking using the *in vitro* tissue sample was significantly more difficult to achieve than with the metal pin target. This was due to the incorrect time-shift values given by the cross-correlation algorithm. Hence, the failed channels had to be manually excluded from the calculations in order to yield the correct displacement estimation values.

The introduced motion-tracking methods cannot be readily used as such during clinical HIFU therapy treatment, because the incorrect time-shift values had to be manually excluded from the calculation algorithm. This process could probably be automated by observing the peak count and the amplitude of the cross-correlation curves. However, this method was not verified in this thesis and hence requires further research about its feasibility.

Keywords: HIFU, Focused Ultrasound, Therapy, Motion-Tracking

AALTO-YLIOPISTO
PERUSTIETEIDEN KORKEAKOULU

DIPLOMITYÖN
TIIVISTELMÄ

Tekijä: Visa Suomi

Työn nimi:

Päivämäärä: 7.8.2012 Kieli: Englanti Sivumäärä:9+52

Teknillisen fysiikan laitos

Professuuri: Teknillinen fysiikka Koodi: Tfy-3

Valvoja: Prof. Esko Kauppinen

Ohjaaja: DI Matti Tillander

Korkeaintensiteettisen fokusoidun ultraääniterapian (HIFU) aikana tapahtuva hengitys vähentää hoidon lämmitystehoa vatsa-alueen elimissä, mikä voidaan kompensoida reaaliaikaisella 3-D -liikkeenkorjauksella. Siksi tässä työssä esitettiin kaksi eri liikkeenseurantamenetelmää, jotka voidaan integroida sellaisenaan Philips Sonalleve MR-HIFU -terapia-alustaan. Näiden menetelmien tarkkuudet mitattiin käyttämällä seurattavina kohteina metallista neulaa sekä kudosnäytettä, joiden avulla mittausdata kerättiin kaikilta liikesuunnilta hyödyntäen yhtä, kolmea ja 32:ta lähettävää ultraäänielementtiä. Lisäksi näiden elementtijoukkojen akustiset kentät simuloitiin, jotta voitiin selvittää esiteltyjen liikkeenseurantamenetelmien teoreettiset rajoitukset käytetyllä HIFU-alustalla.

Liikkeenseurantatarkkuudet eivät eronneet merkittävästi kahden esitetyn menetelmän välillä, vaan tarkkuus oli ennemminkin riippuvainen käytetyn elementtijoukon koosta sekä ultraäänikeilan suunnasta. Pienemmän elementtijoukon käyttäminen ja ultraäänikeilan asennon oikea määrittäminen paransivat saatujen mittaustulosten toistettavuutta. Liikkeenseuranta käyttäen kohteena kudosnäytettä oli huomattavasti vaikeampaa kuin metallineulan seuraaminen, mikä johtui ristikorrelaatioalgoritmin antamista vääristä aika-arvoista. Tämän takia ne piti manuaalisesti poistaa laskennasta oikean tuloksen saamiseksi.

Esitettyjä liikkeenseurantamenetelmiä ei voida sellaisenaan hyödyntää kliinisessä HIFU-terapiassa, koska väärät aika-arvot piti manuaalisesti poistaa laskenta-algoritmista. Tämä prosessi olisi mahdollisesti voitu automatisoida seuraamalla ristikorrelaatiokäyrien huippumääriä ja amplitudeja. Kyseistä menetelmää ei kuitenkaan verifioitu tässä työssä, minkä takia vaadittaisiin lisätutkimuksia sen toteuttamiskelpoisuudesta.

Avainsanat: HIFU, Fokusoitu ultraääni, Terapia, Liikkeenseuranta

Preface

First of all I would like to thank my thesis instructor M.Sc. Matti Tillander for his excellent and patient guidance throughout this project at Philips Medical Systems MR Finland. I also would like to acknowledge M.Sc. Matti Lindström for his advices in developing the software for the measurements.

I am also grateful to my manager D.Sc. Reko Vuorinen for giving me the possibility to conduct the research work for the thesis at Philips. Furthermore, Prof. Esko Kauppinen deserves my gratitude for his efforts in improving the scientific value of the thesis.

The knowledge and experience that I have gained when working with such talented and motivated people will be a big advantage for me in the future.

Espoo, 7.8.2012

Visa Suomi

Contents

Symbols and abbreviations

Symbols

$\mathbf{A}$	One-dimensional displacement matrix of $\vec{a}_i$ where $i \in \{1...8\}$
$\mathbf{A}^+$	Pseudoinverse of $\mathbf{A}$
A	Reduced amplitude of an ultrasound wave
A_0	Unattenuated amplitude of an ultrasound wave
$\vec{a}_i$	One-dimensional displacement vector
$\hat{a}_i$	Unit vector of $\vec{a}_i$
a_{ix}, a_{iy}, a_{iz}	x-, y- and z-components of $\vec{a}_i$
α	Attenuation coefficient
B_0	Main magnetic field strength
B_{loc}	Local magnetic field
C_{A}	Equation constant
C_{B}	Equation constant
C_{C}	Equation constant
c	Sound velocity in an acoustic medium
c_{W}	Sound velocity in water
$\mathbf{D}$	Diagonal matrix in singular value decomposition
$\mathbf{D}^+$	Pseudoinverse of $\mathbf{D}$
$\mathbf{d}$	Displacement $\vec{d}$ in vector form
$\vec{d}$	Three-dimensional displacement vector
d_x, d_y, d_z	Displacement in x-, y- and z-directions
δ	Chemical shift
δ_0	Chemical shift due to magnetic field inhomogeneities
δ_T	Chemical shift due to temperature
E	Energy
γ	Gyromagnetic ratio
i	Index of the variable in a set
$\hat{i}, \hat{j}, \hat{k}$	Unit directional vectors of the x-, y- and z-axes
$\vec{k}$	Wave vector
λ	Ultrasound wavelength
$\mathbf{M}$	Matrix quantity
$\mathbf{M}^+$	Pseudoinverse of $\mathbf{M}$
N	Number of observations
n	Index of a transducer surface element in simulations
ν	Frequency of an ultrasound pulse
ω_0	Precessional frequency of a nuclei
P	Sound pressure of the acoustic field
Φ	MR image phase information
Q_i	Distance travelled by the ultrasound pulse to the element i
R	Equation constant
R_0	Distance from the transmitting element to sonication target

$R_{1,2}$	Reflection coefficient
R_{F}	Distance to the transducer focus point from the elements
$\vec{r}$	Vector indicating the calculation point in simulations
S	Surface area of an element
dS	Infinitesimal surface integration point
ρ	Density of the acoustic medium
T	Temperature
T_{ref}	Reference temperature
T_{E}	Spin echo time
TD_{43}	Thermal dose
$\mathbf{t}$	Time-shift vector of t_i where $i \in \{1...8\}$
t, τ	Time
t_i	Time-shift of an ultrasound pulse between reference and shifted position
$\hat{\theta}_i$, θ_i	Predicted and observed value in RMSE
θ, φ, f	Spherical coordinates
$\mathbf{U}$	Matrix in singular value decomposition
$\mathbf{U}^\top$	Matrix transpose of $\mathbf{U}$
$\mathbf{u}_{\mathrm{A}}$	Vector quantity
$\mathbf{u}_{\mathrm{B}}$	Vector quantity
u	Velocity of transducer surface
$\mathbf{V}$	Orthogonal matrix in singular value decomposition
$\mathbf{V}^\top$	Matrix transpose of $\mathbf{V}$
$\mathbf{v}_{\mathrm{A}}$	Vector quantity
$\mathbf{v}_{\mathrm{B}}$	Vector quantity
x	Distance travelled by an ultrasound wave
$\mathbf{x}_{\mathrm{F}}$	Transducer focus point coordinate vector
X, Y, Z	Rotated coordinate frame in simulations
x, y, z	Calculation point of an acoustic field in simulations
$x_{\mathrm{F}}, y_{\mathrm{F}}, z_{\mathrm{F}}$	Transducer focus point coordinates
x_i, y_i, z_i	Transducer element coordinates
$x_{\mathrm{S}}, y_{\mathrm{S}}, z_{\mathrm{S}}$	Coordinates of a transducer surface element
$\mathbf{x}_{\mathrm{T}}$	Target location coordinate vector
$x_{\mathrm{T}}, y_{\mathrm{T}}, z_{\mathrm{T}}$	Sonication target location coordinates
Z_{A}	Acoustic impedance
Z_{matching}	Acoustic impedance of matching layer
Z_{medium}	Acoustic impedance of acoustic medium
Z_{piezo}	Acoustic impedance of piezoelectric material
Z_1, Z_2	Acoustic impedances of two different media

Abbreviations

CT	Computerised Tomography
EM	Equivalent Minute
HIFU	High-Intensity Focused Ultrasound
MRI	Magnetic Resonance Imaging
MR-HIFU	Magnetic Resonance guided High-Intensity Focused Ultrasound
PRF	Proton Resonance Frequency
RMSE	Root-Mean-Square Error
RX	Receiving channel
TX	Transmitting channel
wt.	Weight

1 Introduction

High-intensity focused ultrasound, or HIFU, is a non-invasive technique for the treatment of tumours in different organs such as uterine [1], liver [2], prostate [3] and breast [4]. In HIFU therapy, the ultrasound beams are focused on a very small area, which produces a rapid local temperature rise. This allows to create irreversible tissue damage to a well-defined focal spot while leaving the surrounding healthy tissue intact. To create thermal damage in a larger scale requires moving the ultrasound focal spot inside the tumour and hence the treatment of large tumours can last several hours [5]. The treatment time is also increased by the cooling periods to avoid excessive skin heating [6].

The long therapy times might not be a problem in organs which are stationary i.e. are not moving inside a human body. However, accurate treatment of human abdominal tumours is difficult because the displacement of abdominal organs due to breathing can be very large when comparing with the size of the focal spot [7]. It is showed that liver and other abdominal organs can move up to 20 mm during a breathing cycle [8] while focal spot is typically 10 mm long and few millimetres wide [1]. This can greatly reduce the efficiency of the heating and hence the creation of thermal damage. Therefore, motion-correction techniques are required to improve the efficacy and reduce the time of HIFU therapy treatment.

The aim of this thesis was to investigate the feasibility of three-dimensional motion-tracking methods for a human liver that could be integrated in Philips clinical magnetic resonance guided HIFU therapy platform (Sonalleve MR-HIFU). A motion-tracking method needs to be robust and accurate in order to be clinically feasible and therefore these aspects were examined. Two motion-tracking techniques were implemented for this purpose: one based on the tracking of temporal shifts in the backscattered ultrasound pulses in eight axial dimensions [7] and the other based on the multistatic radar system used widely in aviation [9]. These two techniques were adapted to the existing Philips Sonalleve MR-HIFU multichannel system and their motion-tracking accuracies were widely investigated and compared to each other. The feasibility of the motion-tracking in liver was examined with *in vitro* tissue samples. Simulations of the acoustic fields were also performed to discuss the theoretical limitations of motion-tracking.

In the following sections first the theoretical basics of biomedical ultrasound physics are introduced and an overview is taken of the history and the current state of HIFU. After this the principles of the two motion-tracking techniques are explained, and the data acquisition equipment used in the actual measurements are presented. The results are examined together with the simulation results, and the accuracies of the two motion-tracking techniques are compared to each other. Finally, the conclusions are made and the possible further research among ultrasound motion-tracking is introduced.

2 Fundamentals of therapeutic ultrasound

2.1 Physics of ultrasound (biomedical perspective)

Mechanical vibrations above the threshold of 20 kHz are called ultrasound which is thus separated from the audible sound by the fact that its spectrum is above the one of human hearing. Ultrasound, like all acoustic waves, are propagating pressure variations i.e. they are travelling microscopic vibrations of atoms and molecules in fluids, solids and lattice structures. Ultrasound cannot therefore propagate in a vacuum but rather requires a physical medium in which to travel. The basic properties of ultrasound waves are wavelength λ, frequency ν and velocity c which relate to each other with (hopefully) familiar equation:

$$\lambda = \frac{c}{\nu} \, . \tag{2.1}$$

There exist four principle modes of ultrasound propagation namely longitudinal, transverse, surface and plate waves. However, longitudinal and transverse waves are the most common types in clinical ultrasound and hence they are further discussed here. Interested reader can refer to [10, 11].

The travelling longitudinal and transverse ultrasonic vibrations are visualized in Fig. 2.1. In longitudinal wave the particle movement is in the same direction with

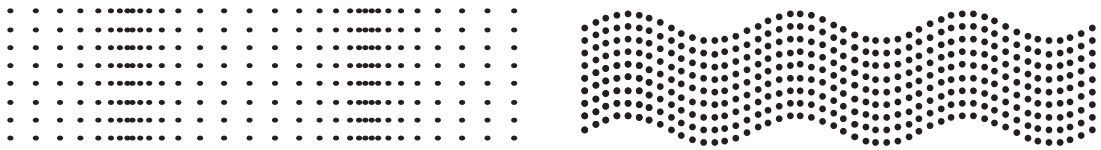

(a) (b)

Figure 2.1: Propagating ultrasound wave (a) in longitudinal mode and (b) in transverse mode. [12]

the propagating wave and they are also sometimes called density waves because their particle density fluctuates as they move. Compression waves can be generated in liquids, as well as in solids, because the energy travels through the atomic structure by a series of compression and expansion movements.

In transverse wave, also called shear wave, the particles move in the direction perpendicular to the wave propagation. Transverse waves require an acoustically solid material for propagation and therefore are not effectively propagating in viscose materials such as fluids. Transverse waves are also relatively weak when compared to longitudinal waves, which is why they are usually simultaneously generated with longitudinal waves while using some of their energy. [10]

The selection of suitable acoustic medium depends on the frequency of the travelling ultrasound wave. Air can act as such medium for ultrasound waves whose frequency is below 1 MHz, but above that the sound transmission in air reduces significantly [13]. However, clinical applications of ultrasound such as diagnostic ultrasound and HIFU usually employ frequencies in the range from 1 MHz to 20 MHz

[14], and therefore require more dense mediums such as water. The shorter wavelength resulting from an increase in frequency will help detecting smaller details in diagnostic ultrasound. For example, human soft tissues consist mainly of water, and therefore, the velocity of sound in it is close to that of water i.e. approximately 1540 m/s [15]. In theory, this would allow details as small as 0.77 mm to be detected with a diagnostic ultrasound device operating at 2 MHz frequency. In practice, however, multiple reflections are interfering with each other, which prevents such accuracy.

When an ultrasound wave propagates through a medium, its intensity decreases with respect to distance travelled. Ultrasonic wave propagation is affected by the microstructure of the medium through which it propagates. *Acoustic attenuation* is a measure of the energy loss of sound propagation in media i.e. the amplitude change of a decaying ultrasound wave. The attenuation is expressed in Nepers per meter (Np/m) or alternatively in dB/m by dividing with 0.1151. It can be calculated with equation:

$$A = A_0 e^{-\alpha x} \tag{2.2}$$

where A_0 is the unattenuated amplitude of the propagating ultrasound wave and A is the reduced amplitude after the wave has travelled a distance x from the initial location. The quantity α is the attenuation coefficient of the wave travelling in the x-direction. The energy of a propagating ultrasound wave is also directly proportional to the square of its amplitude:

$$E \propto A^2 \tag{2.3}$$

which is usually converted into the heat energy of the acoustic medium i.e. vibrational and rotational movements of the molecules.

There are three notable physical effects which cause ultrasound attenuation: scattering, absorption and reflection. Scattering is a general physical process where moving ultrasound wave is forced to deviate from the direction of propagation by the non-uniformities present in the medium through which they pass. In absorption the propagating ultrasound wave loses part of its mechanical energy to the medium. When an ultrasound wave propagates through the body, the absorption process generates heating of the tissue. The same mechanism is also used in HIFU to produce localized thermal damage to a small area. Reflection is the change in direction of a wavefront at an interface between two different media (for example between bone and soft tissue) so that at least part of the wavefront returns into the medium from which it originated. [11, 16]

Attenuation coefficients are used to quantify different media according to how strongly the transmitted ultrasound amplitude decreases as a function of frequency. In general, attenuation is proportional to the square of sound frequency. Ultrasound attenuation also varies depending on the type of the tissue: water has minimal attenuation to ultrasound at 1 MHz, namely 0.0022 dB/cm/MHz. The difference is significant when comparing to the values of muscle (1.57 dB/cm/MHz) and breast (0.75 dB/cm/MHz) for example. [16] These organs thus appear darker in diagnostic ultrasound because the intensity of the reflected ultrasound pulses is lower. In HIFU the high attenuation along the path of propagating ultrasound waves reduces the efficiency of tissue heating in the focus point because most of the kinetic energy is

lost on the way. On the contrary, the high attenuation in the focal spot improves the absorption of kinetic energy and hence increases the efficiency of heating.

Another important quantity in the biomedical ultrasound research is the *acoustic impedance*:

$$Z_{\mathrm{A}} = \rho c \tag{2.4}$$

where ρ is the density of an acoustic medium and c is the corresponding sound velocity. Acoustic impedance is expressed in MRayls and it is important in the determination of acoustic transmission and reflection at the intersection of two media which have different acoustic impedances. If there is a difference in acoustic impedances of the materials on each side of the boundary, part of the propagating ultrasound waves is always reflected at this location. Hence, to ensure efficient propagation of ultrasound waves into tissue in clinical applications, it is necessary to use a contact material whose acoustic impedance is similar.

The rate of the propagating wave intensity that is reflected at the boundary of two different media can be calculated with the equation:

$$R_{1,2} = \left(\frac{Z_2 - Z_1}{Z_2 + Z_1} \right)^2 \tag{2.5}$$

where Z_1 and Z_2 are the corresponding acoustic impedances. Multiplying the reflection coefficient by 100 gives the amount of energy reflected as a percentage with respect to the original energy. The greater the impedance difference is between two media, the greater the percentage of energy will be reflected at the interface. [10] For example, in fat-muscle interface approximately 1% of the mechanical ultrasound energy is reflected back because the acoustic impedances are close to each other (1.38 MRayl vs. 1.70 MRayl respectively [17]). Significantly larger value is achieved in tissue-bone interface where as much as 42% of the incident energy is reflected. This is because the acoustic impedance of bone (7.80 MRayl) differ greatly from the average value in human soft tissue (1.65 MRayl) [17, 18].

Till now we have considered only single propagating ultrasound plane wave and its fundamental properties. However, the ultrasound that is emitted in clinical applications is not usually plane wave like, but rather has a complex structure originated from different sources. Hence, before moving to the next section introducing the production of ultrasound, it is necessary to know how multiple ultrasound waves interact with each other.

When two or more ultrasound waves propagate at the same medium, the net amplitude at each point is the sum of the amplitudes of the individual waves as demonstrated in Fig. 2.2 with one-dimensional transverse waves. This is called the *superposition principle* and it applies to all linear systems. In physics, however, the phenomenon in which two waves superimpose to form a resultant wave is referred as *interference*. The situation where the amplitude of a resultant wave is bigger than either of the two original amplitudes is called *constructive interference*. In Fig. 2.2(a) is visualized the constructive interference with two identical waves which are completely in phase, and therefore, the resulting wave has twice the amplitude of the original waves. The sum of two waves can also be less than either of the waves

interfering with each other. This situation is called *destructive interference* and it is shown in Fig. 2.2(b) for two identical propagating waves whose phase difference is π. The resulting wave thus vanishes i.e. the superimposed amplitude is zero. These two cases are the extremes and in reality the phase difference can be anything between 0 and 2π, which results in various waveform shapes. [10, 19]

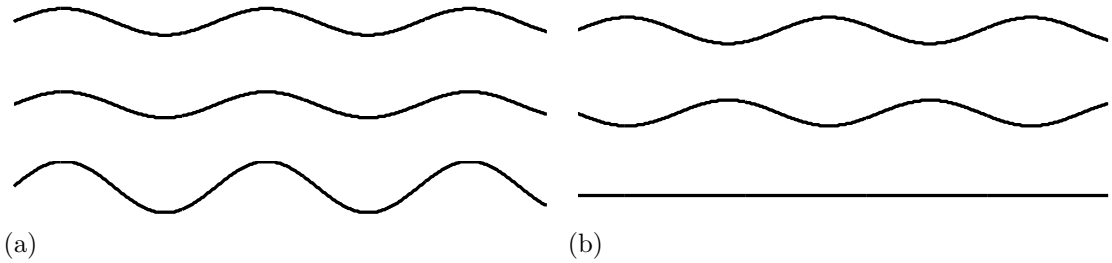

Figure 2.2: Two propagating waves in (a) constructive interference and (b) destructive interference.

Until now we have considered waves in one-dimension only. However, the same principles apply to waves in two and three dimensions as well, and in reality the wave front of a propagating ultrasound wave is actually circular. The circular wave front can be demonstrated by dropping an item, a stone for example, in a pool of water. The waves produced this way radiate out from the source with a circular wave front. In a similar manner, the ultrasound waves radiate from the surface of their source in three dimensions.

When multiple sources are used, which is often the case in HIFU and clinical ultrasound, the waves interact with areas of constructive and destructive interference. This creates areas of higher and lower intensities in the acoustic field, which are referred as *ultrasound beams*. In this fundamental property, the HIFU therapy is also based on. [10]

2.1.1 Definition of ultrasound speckle

When a propagating ultrasound wave is reflected from a scatterer or a cluster of scatterers, its originally sinusoidal shape, or pattern, is modified depending on the structure of the scatterers. The ultrasound pulse reflected from these scatterers has typically a pattern which looks somewhat random, but it is actually unique and characteristic to the structure of the scatterers. This is called the *ultrasound speckle*. The speckle is also dependent on the spatial location of the scatterers in the acoustic medium, and therefore, can be used as the fixed reference point in the ultrasound based motion-tracking techniques.

This property is also utilized in the motion-tracking techniques introduced in this thesis by tracking the speckles reflected from at least three different spatial locations in tissue. These scatterer locations thus act as reference points, which allows to calculate the three-dimensional displacement accurately. However, the problem typically encountered is finding a speckle from the received ultrasound

pulse, because the signal usually contains noise and other artefacts which make the recognition of a speckle difficult.

2.2 Production of ultrasound

The conversion of electric signals to mechanical vibrations whereas the conversion of mechanical vibrations back into electricity is the basis of ultrasonic equipment. In most clinical applications ultrasound is produced by the phenomenon of *piezoelectricity* which means electricity produced by pressure. The piezoelectric effect is a reversible process and it is divided in the *direct piezoelectric effect* and the *reverse piezoelectric effect* both of which are presented in Fig. 2.3.

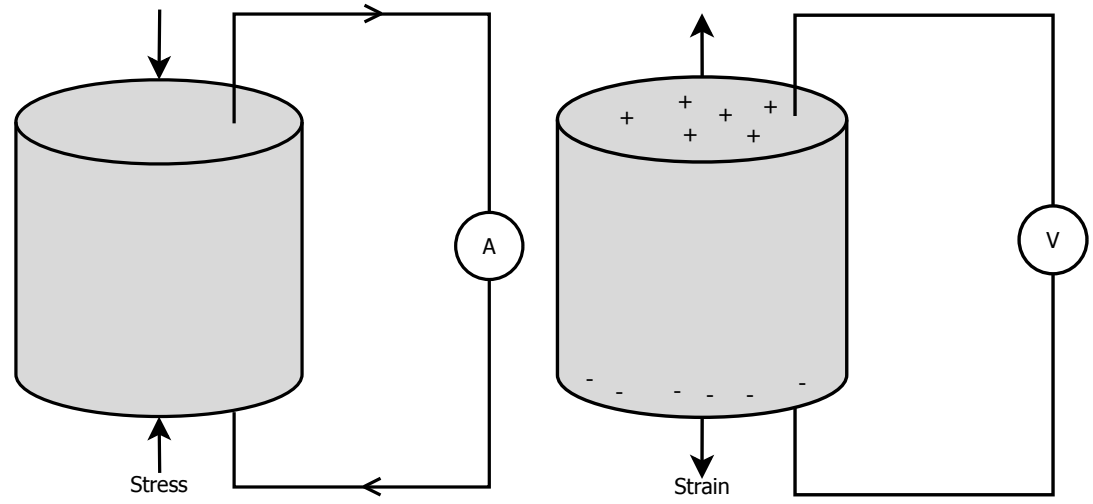

Figure 2.3: (a) Direct piezoelectric effect: applied mechanical stress induces a potential difference i.e. electric field between electrodes. (b) Reverse piezoelectric effect: externally applied electric field causes the material to change dimensions.

The direct piezoelectric effect is a characteristic property of some anisotropic materials in which a mechanical stress causes an inhomogeneous distribution of electric charge inside the material. This imbalance of charges induces a potential difference between the electrodes and makes the current flow in an external electric circuit where the signal is produced. Therefore, it can be used to acquire ultrasound reflections i.e. pressure fluctuations which in turn induce an observable electric signal. [11, 17]

The same process works also in other direction when an externally applied electric field makes the material change dimensions. This phenomenon is called the reverse piezoelectric effect and it is a property of all dielectric materials that causes them to change their shape under an applied electric field. When a voltage is applied on both sides of the material, the polarized molecules will align themselves parallel with the electric field. This results in induced dipoles within the structure of the material and the alignment of molecules will cause the material to deform. Because

the process is reversible, the material returns to its original shape when the electric field is turned off. [10]

The materials which exhibit the properties of direct and reverse piezoelectric effects are called *piezoelectric materials*. The piezoelectric effect occurs only in non-conductive materials which can be either natural or synthetic. They can be divided into two main groups: crystals, which include natural crystals such as quartz (SiO_2) and ceramics, which include synthetic ceramics such as barium titanate ($BaTiO_3$). Nowadays piezoelectric ceramics have become the dominant material for ultrasonic devices due to their good piezoelectric properties and ability to manufacture into various shapes and sizes. [10]

The applied external electric field can also vary in time with certain frequency, which causes the exposed piezoelectric material to vibrate with the same frequency. This direct piezoelectric effect can be utilized to produce ultrasound waves with desired frequencies by generating corresponding external electric field to a piezoelectric material. When the material is put in an appropriate acoustic medium, for example water, it transfers the mechanical vibrations into propagating ultrasonic waves.

2.2.1 Ultrasound transducer

A device that changes electrical energy to acoustic waves or vice versa is called *transducer*. Cross-section of a typical transducer element is presented in Fig. 2.4. The

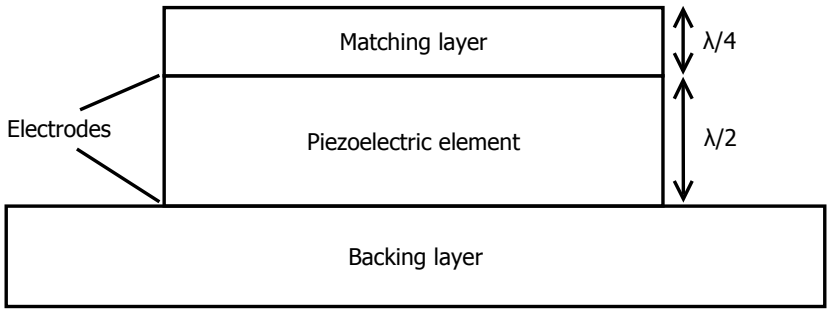

Figure 2.4: Cross-section of a single element transducer.

thickness of an active piezoelectric element is determined by desired central operating frequency of a transducer. A piezoelectric element vibrates with a wavelength that is twice its thickness, and therefore, they are manufactured to the thickness of $\lambda/2$ i.e. half of the desired ultrasound wavelength. The higher is the central operating frequency of the transducer, the thinner the piezoelectric elements have to be. [10] Clinical ultrasound usually employs frequencies between 1 MHz and 20 MHz [14], which correspond to the piezoelectric element thickness between 4.0 mm and 0.2 mm in a transducer made of barium titanate (longitudinal sound velocity $\approx$ 4000 m/s [20]).

In clinical applications, the transducer is in a direct contact with the skin in diagnostic ultrasound, or in HIFU, with the surrounding acoustic medium (normally water [21]). Either way, the acoustic impedance of the piezoelectric elements usually

differ significantly from the target, which would lead to high reflection of ultrasound waves according to Eq. (2.5). Hence, a *matching layer* is required between the transducer and the surrounding acoustic medium in order to improve the ultrasound transmission at the interface. The matching layer is usually made from a material that has an acoustic impedance between the piezoelectric element and the target material i.e. skin or water. The acoustic impedance of a matching layer is often the geometric average of the two acoustic impedances:

$$Z_{\text{matching}} = \sqrt{Z_{\text{piezo}} Z_{\text{medium}}} \tag{2.6}$$

where Z_{piezo} and Z_{medium} are the acoustic impedances of piezoelectric material and acoustic medium, respectively. Optimal transmission of ultrasound pulses is achieved when the matching layer thickness is $\lambda/4$ i.e. one fourth of the desired ultrasound wavelength. This keeps the waves that were reflected back to the matching layer in phase till they eventually exit the layer. [10]

Behind the piezoelectric elements in a transducer is the *backing layer*. The material in this layer is used support the piezoelectric element and to reduce vibrations of the element after pulse excitation. Therefore, it affects the damping characteristics of a transducer i.e. the length of the transmitted ultrasound pulse in cycles. In order to generate short ultrasound pulses, heavier backing layer is needed than with long pulses. If the acoustic impedance of a backing material is similar to that of the piezoelectric element, the most effective damping is produced. Such a transducer will have a wide frequency bandwidth but poor energy transmission efficiency. On the contrary, if the mismatch in impedance between the piezoelectric element and the backing material is large, the ultrasound transmission in the target is increased but with the cost of reduced bandwidth. [10] Air is generally used as backing material in HIFU transducers.

Several factors have to be taken into account when designing a transducer for clinical applications. Parameters such as the material, the mechanical and electrical construction and the aperture size i.e. the area of the element all affect the central operating frequency and the acoustic field of the transducer [10]. These properties have to be chosen specifically for the desired therapy outcome in HIFU. For example, a large enough aperture is needed to distribute the ultrasound energy evenly across the skin in order to avoid undesired skin heating [22].

The desired frequency range of a transducer depend mainly on its application. Lower frequencies (0.5 MHz – 2.25 MHz) allow greater penetration into a target, which is desirable in HIFU therapy. On the other hand, high frequency transducers (15.0 MHz – 25.0 MHz) have lower penetration depth but the short wavelength can offer a greater sensitivity small details, which would count as an advantage in diagnostic ultrasound. [10]

The acoustic field of a transducer can originate from a single transmitting element, but in most cases multiple piezoelectric elements are used. Since the acoustic field is emitted from several points along the surface of a transducer, the ultrasound intensity along the beam is modified by constructive and destructive wave interference as discussed in the end of section 2.1. The structure of acoustic field of a transducer depends on the size of the transducer and its central frequency. In

general, it can be said that when the frequency of ultrasound pulses decreases and the transmitting element size gets smaller, the shape of the emitted acoustic field becomes wider and more spherically shaped. Conversely, when the element size and the frequency of propagating ultrasound pulses increases, the field becomes more directed and beam-like shaped.

It also have to be noted, that the ultrasound beam originating from the transducer does not transfer all of its energy in the direction of wave propagation but rather diverges with a spherical three-dimensional wave front. In order to modify the shape of an acoustic field, piezoelectric materials can be formed in several shapes to create different kinds of transducers for clinical applications. For example, in diagnostic ultrasound a convex shape is typical geometry for a transducer because it produces wide ultrasound field and hence the acquired image will cover a large area. Complete opposite approach is used in the case of HIFU where focusing of ultrasound waves is desired, and therefore, the transducers are formed in concave and spherical shape presented in Fig. 2.5.

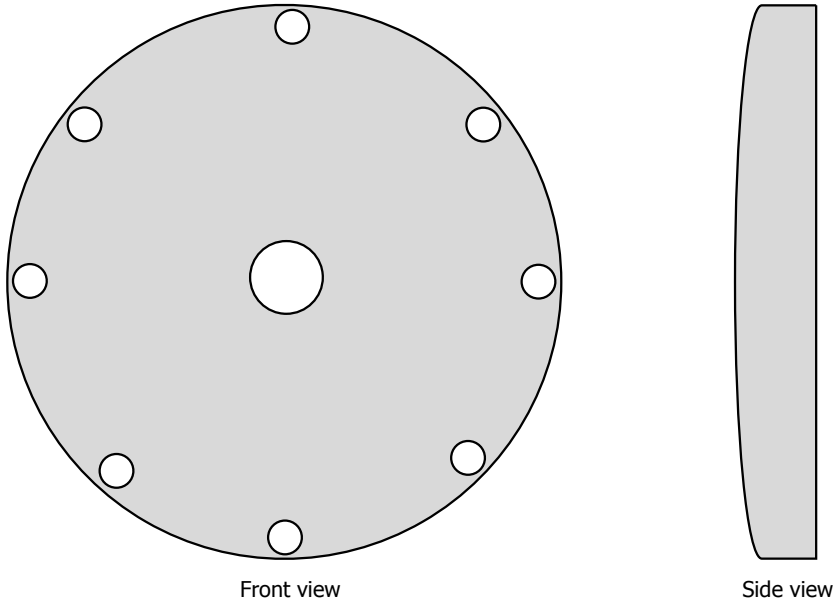

Figure 2.5: Typical geometry of a focusing transducer used in HIFU. The grey area consists of one or multiple transmitting piezoelectric elements. The white elements on the edges are used to receive ultrasonic reflections and the single element in the middle can be used for detecting cavitation.

Typical design for a HIFU transducer is a spherical shaped geometry consisting only of a single piezoelectric element [22]. However, in this case the electronic steering of focal point is not possible and the transducer has to be moved mechanically in order to ablate larger volumes in fibroids. HIFU transducers can also be designed as phased arrays to increase the flexibility and efficiency of HIFU therapy [23, 24]. The increased flexibility in a multielement transducer is achieved by altering the phase of the electric signal for each element individually. By chancing the relative

phase of the elements it is possible to electronically steer the focus away from the geometrical focus of the transducer. The range in which the electronic steering can be altered is limited by the aperture of individual elements [21]. The size of the transducer elements typically varies between 2 mm and 10 mm in diameter [23, 22], which allows the focus point to be steered 20 mm along the beam axis and ± 10 mm to ± 20 mm perpendicularly to the beam axis away from the geometrical focus [23, 25]. For example, in Sonalleve MR-HIFU the diameter of the transducer elements is 6.6 mm. The electronic steering causes a drop in maximum intensity and also deforms the shape of the focal spot [21].

In general, phased array transducers consist of multiple piezoelectric elements each of which is guided with an electric signal whose phase and amplitude are individual. For example, in Sonalleve MR-HIFU the phased array transducer consists of 256 transmitting piezoelectric elements and eight receiving elements, which are used to receive backscattered reflections. In addition to phased array transducer, several other geometries are available for different applications such as the treatment of brain tumours [22].

2.3 History and physical principles of HIFU

The motivation for the invention of HIFU therapy was to develop a reliable and minimally-invasive alternative to open surgery. Currently, the only widespread non-invasive methods for cancer treatment (in addition to HIFU) are chemotherapy and radiotherapy, both of which carry significant risks of side-effects such as exposure to large amounts of ionising radiation [14]. Hence, HIFU has the potential to provide the clinicians with another non-invasive, targeted treatment option.

In HIFU the mechanical ultrasound waves transmitted by the spherical shaped transducer propagate through skin into the body and are focused to a small high-intensity focal spot. The ultrasound waves focused in this small area produce a rapid local temperature rise while keeping the intensity low in the surrounding areas. This allows to create irreversible tissue damage to a well-defined focal spot while leaving the surrounding healthy tissue intact. In general, the frequency used in the high-intensity ultrasound therapies varies between 0.8 MHz and 4.0 MHz [21].

The physical effects of high-intensity ultrasound on biological tissue were first studied in 1927 by Wood and Loomis [26], but at that time HIFU did not gain widespread clinical use as hyperthermia or tissue ablation therapy method due to the lack of suitable guidance and monitoring methods. For example, the non-invasive temperature monitoring of the HIFU therapy was not possible, and therefore, the induced thermal damage could only be approximated. Also the location of the target tumour was not exactly known due to the lack of real-time anatomical information. However, different clinical applications of HIFU therapy were continued to study during the following decades such as the ablation of central nervous system [27, 28].

For HIFU therapy treatment, it is crucial to monitor the temperature in the treatment position accurately in order to treat the tumour while sparing the surrounding healthy tissue. This is difficult however, because the heat diffusion, absorption and perfusion of the tissue vary depending on its microstructure, density,

local physiological parameters and temperature [21]. This makes predicting the temperature distribution in the target difficult, which requires continuous temperature monitoring during the treatment.

The potential of combining the temperature and anatomy information provided by MRI scanner to give real-time feedback for HIFU therapy, namely Magnetic Resonance guided HIFU or MR-HIFU, was first suggested by Cline et al. in 1992 [29]. The advantages of MRI are its non-invasive imaging modality and good soft-tissue contrast. The tissue parameters in MRI are altered due to the ablation and hence it is possible to track the severity and extent of the desired thermal damage. MRI provides also real-time *in vivo* temperature information [30, 31], which is crucial for controlling the area of the tissue damage. It is also possible to guide HIFU therapy by monitoring the bubble activity i.e. cavitation and boiling during the treatment [32, 33, 34].

Although HIFU has several advantages over the other non-invasive cancer therapy methods, it has also its limitations. Ultrasound cannot propagate through air filled organs such as lung, and other obstructions such as bone and skull can absorb or reflect an ultrasound beam. For this reason tumours of the lung or bowel whereas tumours lying in close proximity to such organs are not likely to be targets for HIFU. Also the treatment times for HIFU therapy session are generally longer than those of radio- or chemotherapy. A typical HIFU therapy treatment time of few hours would be acceptable when compared with alternative of surgical operations, but is significantly longer to other minimally invasive options.

HIFU has already accepted treatment modality for uterine fibroids and bone pain palliative therapy in e.g. Europe and USA. In China ultrasound guided HIFU is already established as such for the treatment of liver and breast cancers in addition to uterine fibroids [14]. The future perspectives for HIFU may provide an alternative surgery method in variety of applications such for the treatment of liver, breast and prostate cancers as the ongoing clinical research further investigates their safety and efficiency aspects.

2.3.1 Temperature monitoring in MR-HIFU

Temperature monitoring in MR-HIFU is based on the phenomenon of Proton Resonance Frequency shift, or PRF shift, which was first discovered by Hindman in 1966 [35]. PRF shift is based on a well-known physical phenomenon where the proton absorbs and emits energy at a specific resonance frequency. This resonance frequency is partly affected by the temperature and therefore, by measuring the shift in the resonance frequency, the temperature change can be determined.

Human body consists mainly of water molecules each of which contains two bonded hydrogen nuclei i.e. protons. When these nuclei are placed in an external magnetic field B_0, they precess with a certain frequency which is called the *Larmor frequency*. This precessional frequency is dependent on the strength of the magnetic field and can be defined by the *Larmor equation*:

$$\omega_0 = \gamma B_0 \tag{2.7}$$

where γ is the gyromagnetic ratio which is a constant unique to every atom ($\gamma = 2\pi \times 42.576$ MHz/T for proton). The magnetic field experienced by the hydrogen nuclei is not however exactly B_0, but is reduced, or *screened*, by the electron clouds of the water other surrounding molecules. The amount of screening depends on the chemical environment of the nuclei, and hence, this phenomenon is called the *chemical shift*. By expressing the chemical shift with the symbol δ, the local magnetic field experienced by the hydrogen nuclei can be written as:

$$B_{\text{loc}} = B_0 + \delta B_0 = (1 + \delta)B_0 \ . \tag{2.8}$$

The chemical shift is partly due to the magnetic field inhomogeneities δ_0 caused by screening, but it also contains a temperature dependent part $\delta_T(T)$:

$$\delta(T) = \delta_0 + \delta_T(T) \ . \tag{2.9}$$

The temperature dependent part is linearly dependent on the temperature, which also creates a linear temperature dependence on the precessional frequency of hydrogen nuclei according to Eq. (2.7) [36]:

$$\omega_0(T) = \gamma B_{\text{loc}} = \gamma(1 + \delta(T))B_0 \ . \tag{2.10}$$

This temperature dependent shift in resonance frequency can be calculated using the phase information from the MR images of a gradient echo sequence [31]:

$$\Phi(T) = \gamma\delta(T)T_{\text{E}}B_0 \tag{2.11}$$

where Φ is the image phase and T_{E} is the echo time of the MR imaging sequence used. However, we cannot obtain the absolute temperature information due to the temperature independent part δ_0 present in the acquired MR phase image. Instead, we have to measure the change in the temperature by eliminating the temperature independent part from the Eq. (2.11). This can be done by subtracting a reference phase image at known temperature T_{ref} from the phase image acquired at T. This allows to calculate the change in the temperature with respect to the known reference temperature:

$$\Delta T = T - T_{\text{ref}} = \frac{\Phi(T) - \Phi(T_{\text{ref}})}{\gamma B_0 \delta_T T_{\text{E}}} \ . \tag{2.12}$$

This temperature dependence can be used to acquire *in vivo* temperature information during the MR-HIFU treatment. [35, 37] Because the PRF technique is only able to calculate the relative temperature with respect to T_{ref}, human body temperature (37 °C) is typically used as the initial reference temperature during the MR-HIFU treatment [21].

2.3.2 Thermal dose

Ultrasound can cause tissue damage by the conversion of mechanical energy into heat. When an ultrasound beam propagates through tissue, its amplitude reduces with respect to distance travelled i.e. attenuates according to Eq. (2.2). Because

the energy of a propagating ultrasound wave is directly proportional to the square of its amplitude, the attenuation can be thought as the energy transform between the ultrasound pulses and the acoustic medium i.e. the tissue.

The attenuation in tissue is caused partially due to scattering and partially due to absorption of kinetic energy [21]. The absorption is caused by the rotational and vibrational motion of the tissue molecules, which induce fluctuations in pressure and leads to a rise in temperature [38]. This converts the kinetic energy of propagating ultrasound pulses to heat energy. The scattering is caused by the homogeneities of the tissue, and it will redirect and disperse the ultrasound waves from their direction of propagation. However, the attenuation and the absorption are often assumed to be the same quantity, since absorption and scattering can difficultly be distinguished and both are related to similar phenomena [1, 38].

Ultrasound waves might also propagate through tissue interfaces, which typically have different acoustic impedances. This causes the reflection of the ultrasound pulses, which will reduce the energy contained in the transmitted ultrasound beam. However, this effect is mostly negligible, because the acoustic impedances of biological soft tissues are usually very similar [15].

When the energy is absorbed as heat though these processes, it will dissipate rapidly in normal circumstances due to diffusion and perfusion. However, if the heating rate exceeds that of cooling, local temperature rise will result. As the measure of thermal damage the concept of *thermal dose* is generally used.

The idea of thermal dose was introduced in 1984 by Sapareto and Downey [39] for defining the severity of thermal damage in tissue. This model does not only take into account the current temperature but also the entire heating history during the thermal therapy in estimating the total thermal damage. The equation for thermal dose is defined as:

$$TD_{43}(t) = \int_0^t R^{(43-T(\tau))} d\tau \tag{2.13}$$

with

$$\begin{aligned} R &= 0.25 \qquad T < 43\ ^\circ\mathrm{C} \\ R &= 0.50 \qquad T \geq 43\ ^\circ\mathrm{C} \end{aligned}$$

where TD_{43} is the thermal dose in equivalent minutes (EM) at 43 °C, t is the time and $T(\tau)$ is the time dependent temperature. The threshold of 240 EM is considered to be a good representative for coagulative necrosis [40, 41] while the limit of 30 EM has been showed to be relevant indicator for onset of tissue damage [40]. The estimation of the tissue thermal damage in Sonalleve MR-HIFU is also based on this dependence.

2.4 Overview of Philips Sonalleve MR-HIFU system

Sonalleve MR-HIFU is as a non-invasive treatment platform for uterine fibroid and bone pain palliative therapies. It uses focused ultrasound waves produced by a transducer to heat and coagulate pathological tissue deep inside the body without

damaging intervening tissue, and combines this with temperature monitoring and anatomical information provided by Magnetic Resonance Imaging (MRI) scanner.

As mentioned earlier, ultrasound waves above approximately 1 MHz cannot propagate long distances in air due to the significant attenuation and rather need an acoustic path in which to travel. Sonalleve MR-HIFU uses two therapy frequencies at 1.20 MHz and 1.45 MHz, and therefore it needs a continuous acoustic path from the transducer to a human body. This is usually accomplished in a clinical HIFU platform by positioning the transducer in a degassed water or oil bath which is sealed inside a MR compatible tabletop using a thin membrane [42, 43, 44]. In Sonalleve MR-HIFU this membrane is made of commercial plastic material called Mylar, which also acts as an acoustic window though which the ultrasound waves are able to propagate into the patient.

The patient is positioned on top of the HIFU tabletop so that the fibroid is located above the acoustic or *sonication* window and is thus reachable by the ultrasound waves. A gelpad is often positioned between the acoustic window and the patient together with distilled water to improve the acoustic coupling between the water tank and the skin of the patient [43, 44]. Air pockets could exist between the patient and the transducer if the gelpad is not placed between them. These air pockets would reflect back part of the ultrasound waves and thus reduce the efficiency of heating.

The heating of desired location i.e. the fibroid is achieved by accurate positioning of the transducer. The transducer positioning system in Sonalleve MR-HIFU has five degrees of freedom (three axial and two rotational) which allow to induce localized thermal damage in the desired target location. The use of phased-array transducer also allows to steer the focus point electronically. The accurate displacements of the transducer are typically provided by software controlled piezoelectric or ultrasound motors [42, 45] which are MR compatible. More information about the Philips clinical HIFU platform can be found from the reference [1].

2.5 Motion-tracking in HIFU

Different motion-tracking methods have been widely investigated for medical applications such as radiotherapy, magnetic resonance imaging (MRI), computerised tomography (CT) and HIFU [46, 47, 48]. These motion-tracking techniques usually rely on radio-frequencies in MRI, x-rays in CT or ultrasound in HIFU to track the displacements of organs in a human body, but different techniques can also be combined. For example, it is possible to use MRI navigator sequences to track motion during HIFU therapy [49].

MRI based motion-tracking methods can be used to track three-dimensional motion but they are usually expensive and slow. The sampling speed can be increased by using fast imaging sequences but this exposes body to large amounts of radio-frequencies which turn into heat when absorbed by a body. X-ray based methods can also be implemented in three-dimensions but they use ionising radiation and thus should be avoided. Also techniques such as respiratory gating have been suggested as a solution for the problem of breathing motion in radiation therapy [50], which

could also be implemented in HIFU. This method however is not relying on the concept of motion correction but rather in preventing the abdominal organ motion during the radiation therapy.

Ultrasound techniques are capable to track three-dimensional motion but the penetration depth is tissue dependent, and therefore, they cannot track organs which are located behind obstacles such as bones or organs which do not give strong enough reflections. The main advantages of ultrasound based methods are their low-cost, good spatial resolution, fast imaging speed and the use of non-ionising radiation. Furthermore, ultrasound based methods can be easily integrated in the existing HIFU therapy systems in real-time using high-frequency sampling [7]. Finally, ultrasound motion-tracking techniques are non-invasive because they rely on natural inhomogeneities in human organs. These inhomogeneity areas can be used as reference markers to track the motion of tissues located deep within organs.

Some of the commercial systems can follow the amplitude of the displacement but not its direction [7], which prevents to compensate the three-dimensional movement in the therapeutic or imaging system. A motion-tracking technique using ultrasound capable of determining both the amplitude and the direction of the movement in real-time have been suggested by Pernot et al. [7]. This technique uses three different axial displacement vectors to yield the correct three-dimensional displacement of a target, and it is also implemented with modifications in this thesis. An another technique used in the motion-tracking is the multistatic radar method, which is also able to track three-dimensional motion by using the several simultaneously acquired reflections. The theoretical principles of these two methods are introduced more extensively in the next section.

3 Materials and methods

3.1 Theory of three-dimensional motion-tracking

3.1.1 Triangulation method

The first method to estimate the target displacement was implemented from the reference [7]. The correct 3-D displacement estimation can be achieved by using at least three 1-D axial displacement measurements i.e. the transmitting element cluster and the receiving element are located in the same transducer sector as seen in Fig. 3.1. Although three element clusters would be enough to yield a three-dimensional

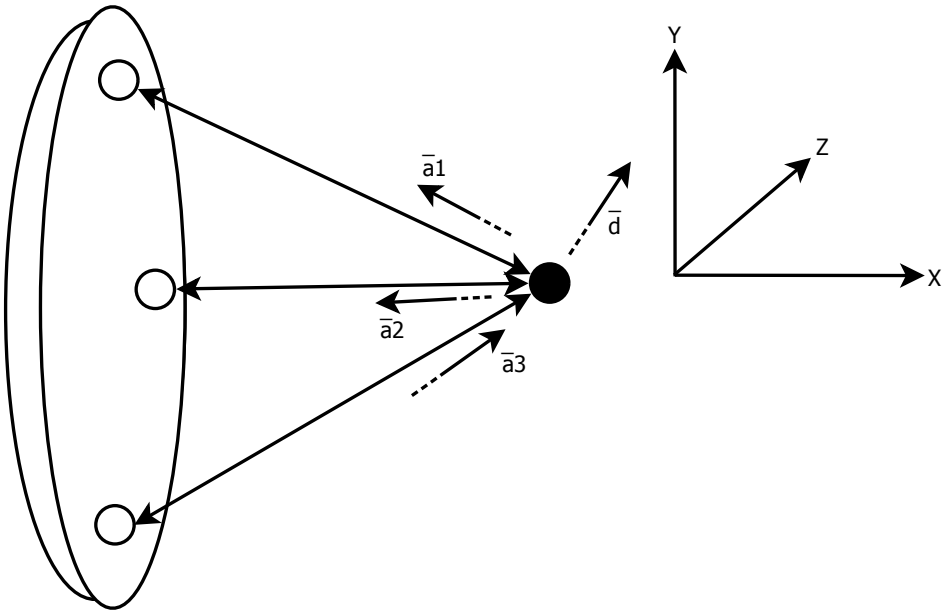

Figure 3.1: The triangulation displacement estimation principle using three tranmitting and receiving elements. The receiving elements give three 1-D axial displacement vectors $\vec{a}_1, \vec{a}_2$ and $\vec{a}_3$ which will define the actual 3-D displacement $\vec{d}$ uniquely by vector sum in the cartesian coordinate frame.

displacement estimate, in the actual measurement eight receiving elements and eight transmitting element clusters were used in order to calculate more stable and accurate displacement estimate.

As mentioned before, in order to calculate the correct displacement vector $\vec{d}$, two subsequent measurements had to be taken: one in the reference position and one in the shifted position. The time-window at the receiving end was delayed so that the desired reflection from the target was in the middle of the sampling window and all the other reflections (for example from the water tank walls) were neglected. This allowed to calculate eight one-dimensional cross-correlations between the corresponding pulses received from the reference and shifted position. The maximum amplitude of the cross-correlation curve will hence tell the time difference t_i between the reflections received from the reference and shifted position.

For receiving element i the time shift could thus be written as:

$$t_i = 2\frac{a_{ix}dx + a_{iy}dy + a_{iz}dz}{c_{\mathrm{W}}} \qquad i \in \{1...8\} \tag{3.1}$$

where a_{ix}, a_{iy} and a_{iz} are the displacements in x-, y- and z-direction for the receiving element i and c_{W} is the sound velocity in water ($\approx$ 1500 m/s at 22.0 °C).

After eight time-shifts t_i were successfully calculated by the cross-correlation, each of them defined the magnitude of the displacement in the direction of vector $\vec{a}_i$. The direction of the vector $\vec{a}_i$ was defined as the view-angle of the element i which is the beam axis of the particular element or element cluster. If we refer to the coordinates of the focus point as $(x_{\mathrm{F}}, y_{\mathrm{F}}, z_{\mathrm{F}})$ and the ith receiving element coordinates as (x_i, y_i, z_i), we get an expression for the unit vector:

$$\hat{a}_i = \frac{(x_{\mathrm{F}} - x_i)\hat{i} + (y_{\mathrm{F}} - y_i)\hat{j} + (z_{\mathrm{F}} - z_i)\hat{k}}{\sqrt{(x_{\mathrm{F}} - x_i)^2 + (y_{\mathrm{F}} - y_i)^2 + (z_{\mathrm{F}} - z_i)^2}} \qquad i \in \{1...8\}\ . \tag{3.2}$$

When we multiply this with the magnitude of the displacement t_i from Eq. (3.1), we obtain eight one-dimensional displacement vectors:

$$\vec{a}_i = t_i \times \hat{a}_i \qquad i \in \{1...8\} \tag{3.3}$$

each of which tells the direction and magnitude of the shift in one dimension corresponding to the view angle of the element i.

As mentioned earlier, the correct displacement $\vec{d}$ could be estimated using only three separate receiving elements. However, in terms of the estimation robustness and stability all the eight receiving elements were used. This gave an overdetermined equation set with 8×3 one-dimensional displacement matrix $\mathbf{A}$, 8×1 time-shift vector $\mathbf{t}$ and the unknown 3×1 matrix $\mathbf{d}$ which tells the actual displacement to be calculated:

$$\mathbf{t} = \frac{2}{c_{\mathrm{W}}}(\mathbf{A} \times \mathbf{d}) \tag{3.4}$$

where

$$\mathbf{t} = \begin{bmatrix} t_1 \\ \vdots \\ t_8 \end{bmatrix} \qquad \mathbf{A} = \begin{bmatrix} a_{1x} & a_{1y} & a_{1z} \\ \vdots & \vdots & \vdots \\ a_{8x} & a_{8y} & a_{8z} \end{bmatrix} \qquad \mathbf{d} = \begin{bmatrix} d_x \\ d_y \\ d_z \end{bmatrix}\ . \tag{3.5}$$

In order to calculate the correct uniquely determined displacement vector $\mathbf{d}$ from this overdetermined linear equation set, the pseudoinverse of the matrix $\mathbf{A}$ was calculated using the singular value decomposition:

$$\mathbf{A} = \mathbf{U} \times \mathbf{D} \times \mathbf{V}^{\top} \tag{3.6}$$

$$\mathbf{A}^{+} = \mathbf{V} \times \mathbf{D}^{+} \times \mathbf{U}^{\top} \tag{3.7}$$

where $\mathbf{U}$ is a 8×3 matrix, $\mathbf{D}$ is 3×3 diagonal matrix, $\mathbf{V}$ a 3×3 orthogonal matrix, $\mathbf{A}^{+}$ and $\mathbf{D}^{+}$ are the pseudoinverse of $\mathbf{A}$ and $\mathbf{D}$, respectively and $\mathbf{V}^{\top}$ and $\mathbf{U}^{\top}$ are the matrix transposes of $\mathbf{V}$ and $\mathbf{U}$, respectively.

This yields the uniquely determined least-squares solution vector:

$$\mathbf{d} = \frac{c_{\mathrm{W}}}{2}(\mathbf{A}^{+} \times \mathbf{t})\ . \tag{3.8}$$

3.1.2 Multistatic radar method

The second method used to estimate the displacement is slightly modified version of the multistatic radar 3-D target location described in the reference [9]. The principle of this method is presented in Fig. 3.2. The idea is to use at least three separate

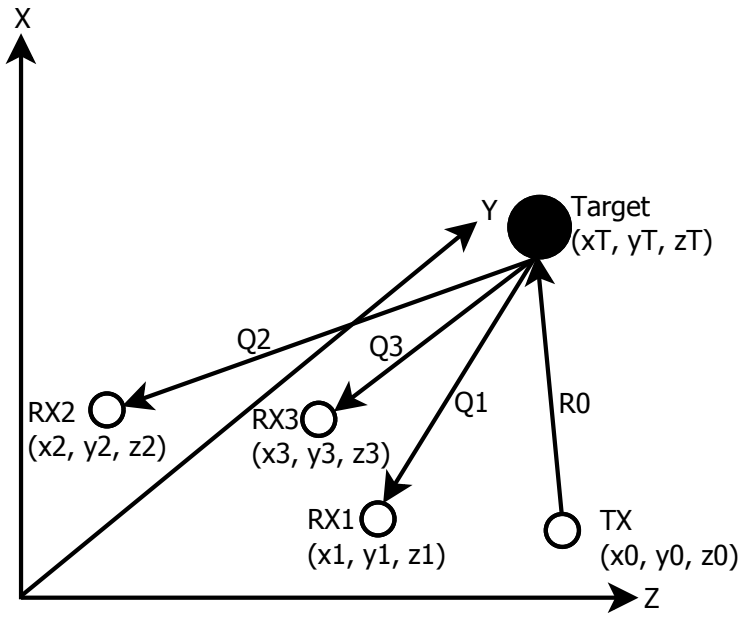

Figure 3.2: Schematic presentation of the target location using multistatic method. Transmitting transducer TX at location (x_0, y_0, z_0) sends an ultrasound pulse whose reflection is received using three separate transducers RX1, RX2 and RX3.

receiving elements (RX1, RX2, RX3) but this time only one transmitting element cluster (TX) compared to the triangulation method presented in section 3.1.1 to solve the correct three-dimensional target location $(x_\mathrm{T}, y_\mathrm{T}, z_\mathrm{T})$.

The basic idea is first to measure the time difference between the transmission of the ultrasound pulse and the reception of the reflection from the sonication target. By knowing the sound velocity in water, we can solve the actual distance travelled by the ultrasound pulse. Again, to improve the stability and robustness of the method we are using seven receiving elements instead of three. All the eight available receiving elements were not used because one of them were right next to the transmitting element cluster.

The use of seven receiving elements yields a set of non-linear equations:

$$\begin{aligned} R_0^2 &= (x_0 - x_\mathrm{T})^2 + (y_0 - y_\mathrm{T})^2 + (z_0 - z_\mathrm{T})^2 \\ (Q_1 - R_0)^2 &= (x_1 - x_\mathrm{T})^2 + (y_1 - y_\mathrm{T})^2 + (z_1 - z_\mathrm{T})^2 \\ (Q_2 - R_0)^2 &= (x_2 - x_\mathrm{T})^2 + (y_2 - y_\mathrm{T})^2 + (z_2 - z_\mathrm{T})^2 \\ &\vdots \\ (Q_7 - R_0)^2 &= (x_7 - x_\mathrm{T})^2 + (y_7 - y_\mathrm{T})^2 + (z_7 - z_\mathrm{T})^2 \end{aligned} \tag{3.9}$$

where Q_i is the the distance travelled by the ultrasound pulse from the transmitting element cluster $i = 0$ via target to the receiving element $i \in \{1...7\}$, R_0 is the unknown distance from the target to the transmitting element cluster and x_i, y_i and z_i are the cartesian coordinate locations for transmitting element cluster $i = 0$, receiving elements $i \in \{1...7\}$ and the target $i = \mathrm{T}$. Hence, in this overdetermined system we have eight non-linear equations and four unknown variables, namely, the distance from the transmitting element cluster to the target R_0 and the target location $(x_\mathrm{T}, y_\mathrm{T}, z_\mathrm{T})$.

Because the cross-correlation gives us the time difference between the two different reflections corresponding to the reference position and shifted position of the target, we must estimate the travelled distances $Q_1 - Q_7$ by employing *a priori* knowledge of the reference target location being in the focus point of the transducer. Thus, by adding the time delays t_i obtained from one-dimensional cross-correlation calculations, we obtain the change in the travelled distance for each of the seven receiving elements:

$$Q_i = \frac{2R_\mathrm{F}}{c_\mathrm{W}} + t_i \qquad i \in \{1...7\} \tag{3.10}$$

where R_F is the distance to the transducer focus point ($R_\mathrm{F} = 0.14$ m) and c_W is the sound velocity in water.

The equation set in Eq. (3.9) is linearised with respect to $R_0, x_\mathrm{T}, y_\mathrm{T}$ and z_T by taking the difference of the subsequent equations which yields:

$$\begin{aligned}
&-Q_1^2 + 2Q_1R_0 - (x_0^2 + y_0^2 + z_0^2) + (x_1^2 + y_1^2 + z_1^2) \\
&\quad = 2(x_1 - x_0)x_\mathrm{T} + 2(y_1 - y_0)y_\mathrm{T} + 2(z_1 - z_0)z_\mathrm{T} \\
&\\
&Q_1^2 - Q_2^2 + 2(Q_2 - Q_1)R_0 - (x_1^2 + y_1^2 + z_1^2) + (x_2^2 + y_2^2 + z_2^2) \\
&\quad = 2(x_2 - x_1)x_\mathrm{T} + 2(y_2 - y_1)y_\mathrm{T} + 2(z_2 - z_1)z_\mathrm{T} \\
&\\
&\qquad \vdots \\
&\\
&Q_6^2 - Q_7^2 + 2(Q_7 - Q_6)R_0 - (x_6^2 + y_6^2 + z_6^2) + (x_7^2 + y_7^2 + z_7^2) \\
&\quad = 2(x_7 - x_6)x_\mathrm{T} + 2(y_7 - y_6)y_\mathrm{T} + 2(z_7 - z_6)z_\mathrm{T}
\end{aligned} \tag{3.11}$$

which we can formulate in matrix form where $\mathbf{v}_\mathrm{A}$ and $\mathbf{v}_\mathrm{B}$ are 7×1 vectors, $\mathbf{M}$ is 7×3 matrix, $\mathbf{x}_\mathrm{T}$ is 3×1 target position vector and R_0 is the unknown distance from the target to the transmitting element cluster as:

$$\mathbf{v}_\mathrm{A} + R_0\mathbf{v}_\mathrm{B} = \mathbf{M} \times \mathbf{x}_\mathrm{T} \tag{3.12}$$

where

$$\mathbf{v}_\mathrm{A} = \begin{bmatrix} -Q_1^2 - (x_0^2 + y_0^2 + z_0^2) + (x_1^2 + y_1^2 + z_1^2) \\ Q_1^2 - Q_2^2 - (x_1^2 + y_1^2 + z_1^2) + (x_2^2 + y_2^2 + z_2^2) \\ \vdots \\ Q_6^2 - Q_7^2 - (x_6^2 + y_6^2 + z_6^2) + (x_7^2 + y_7^2 + z_7^2) \end{bmatrix} \tag{3.13}$$

$$\mathbf{v}_{\mathrm{B}} = \begin{bmatrix} 2Q_1 \\ 2(Q_2 - Q_1) \\ \vdots \\ 2(Q_7 - Q_6) \end{bmatrix} \tag{3.14}$$

$$\mathbf{M} = \begin{bmatrix} 2(x_1 - x_0) & 2(y_1 - y_0) & 2(z_1 - z_0) \\ 2(x_2 - x_1) & 2(y_2 - y_1) & 2(z_2 - z_1) \\ \vdots & \vdots & \vdots \\ 2(x_7 - x_6) & 2(y_7 - y_6) & 2(z_7 - z_6) \end{bmatrix} \tag{3.15}$$

$$\mathbf{x}_{\mathrm{T}} = \begin{bmatrix} x_{\mathrm{T}} \\ y_{\mathrm{T}} \\ z_{\mathrm{T}} \end{bmatrix} \ . \tag{3.16}$$

By solving the pseudoinverse of the matrix $\mathbf{M}$ with singular value decomposition Eq. (3.6) and treating the unknown parameter R_0 as independent variable, we obtain:

$$\mathbf{x}_{\mathrm{T}} = \mathbf{M}^{+} \times (\mathbf{v}_{\mathrm{A}} + R_0 \mathbf{v}_{\mathrm{B}}) = \mathbf{u}_{\mathrm{A}} + R_0 \mathbf{u}_{\mathrm{B}} \ . \tag{3.17}$$

To solve the unknown parameter R_0, we substitute the expression for $\mathbf{x}_{\mathrm{T}}$ from Eq. (3.17) into the topmost equation in Eq. (3.9) to yield a quadratic equation for R_0:

$$C_{\mathrm{A}} R_0^2 + C_{\mathrm{B}} R_0 + C_{\mathrm{C}} = 0 \tag{3.18}$$

where

$$C_{\mathrm{A}} = \mathbf{u}_{\mathrm{B}}(1)^2 + \mathbf{u}_{\mathrm{B}}(2)^2 + \mathbf{u}_{\mathrm{B}}(3)^2 - 1 \tag{3.19}$$

$$C_{\mathrm{B}} = 2\mathbf{u}_{\mathrm{B}}(1)(\mathbf{u}_{\mathrm{A}}(1) - x_0) + 2\mathbf{u}_{\mathrm{B}}(2)(\mathbf{u}_{\mathrm{A}}(2) - y_0) + 2\mathbf{u}_{\mathrm{B}}(3)(\mathbf{u}_{\mathrm{A}}(3) - z_0) \tag{3.20}$$

$$C_{\mathrm{C}} = (\mathbf{u}_{\mathrm{A}}(1) - x_0)^2 + (\mathbf{u}_{\mathrm{A}}(2) - y_0)^2 + (\mathbf{u}_{\mathrm{A}}(3) - z_0)^2 \ . \tag{3.21}$$

We can now solve the two roots for R_0 from the quadratic Eq. (3.18):

$$R_0 = \frac{-C_{\mathrm{B}} \pm \sqrt{C_{\mathrm{B}}^2 - 4C_{\mathrm{A}}C_{\mathrm{C}}}}{2C_{\mathrm{A}}} \tag{3.22}$$

and by substituting these roots to Eq. (3.17), we can solve two solutions for three dimensional target position $\mathbf{x}_{\mathrm{T}} = (x_{\mathrm{T}}, y_{\mathrm{T}}, z_{\mathrm{T}})$, one of which represents the correct position. The correct target position can be obtained by investigating the x-coordinates (vertical direction) of the two solutions and the incorrect one will suggest a target position which is physically impossible i.e. below the transducer.

Because we wanted to know the shift instead of the actual position, we must reduce the coordinates of our approximation i.e. the transducer focus point $\mathbf{x}_{\mathrm{F}} = (x_{\mathrm{F}}, y_{\mathrm{F}}, z_{\mathrm{F}})$ from the obtained solution which finally will yield the actual shift:

$$\mathbf{d} = \mathbf{x}_{\mathrm{T}} - \mathbf{x}_{\mathrm{F}} \ . \tag{3.23}$$

3.2 Data acquisition and measurement equipment

The measurement setup is presented in Fig. 3.3. A computer controlled three-axis motor drive consisting of three high-precision stepper motors (Newport), normally used for hydrophone measurements [51], was used to accurately move the sonication target inside the water tank. The tank was filled with distilled and degassed water and it was placed on top of the MR-HIFU tabletop (Philips Sonalleve V2) so that the 256-channel phased-array transducer (Philips Ultrasound SX-140) was straight below it. The transducer was positioned in the upper position close to the Mylar membrane which acted as the sonication window in order to avoid reflections from it. These reflections could have caused artefacts in the acquired data and hence disturb the data analysis.

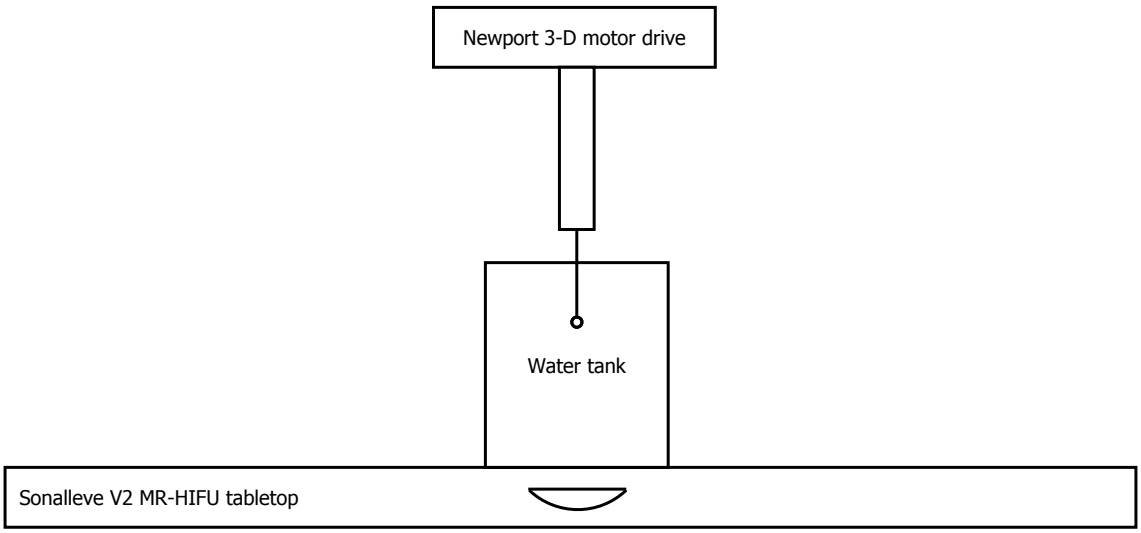

Figure 3.3: Schematic presentation of the measurement setup. Water tank was positioned on top of the MR-HIFU tabletop and a three-axis motor drive was used to move the sonication target inside the tank. The transducer was located inside the tabletop straight underneath the water tank.

Two different sonication targets were used. To verify the accuracy of the method, a sewing pin was used because of its symmetric ball shape and the hard material (plastic) and thus it was able to act as an almost ideal ultrasound reflector. In an ideal reflector the ultrasound pulses reflected from it will have the same sinusoidal waveform as in the transmitted pulses.

The second target was a large piece of pork meat with size approximately 15 $\times$ 10 $\times$ 10 cm^3. It was placed inside a Minigrip bag containing distilled and degassed water with 1%-wt. NaCl in order to avoid cell expansion due to osmosis. It was positioned so that the muscle fibres were in the horizontal direction in order to maximize the reflections from them. The reflections received from this type of inhomogeneous tissue are speckles (see section 2.1.1) because they do not have the sinusoidal shape of the transmitted pulses. The aim of this target was to validate the accuracy of the method for the liver application.

The ultrasound pulses used in the experiment were designed to have the peak acoustic power of 2 W at maximum and 10-cycle sinusoidal pattern which was the shortest available pattern that the system was capable of. The frequency of the pulses was set to 1.20 MHz which is the typical frequency used in HIFU therapy treatments.

The diameter of the phased array transducer was 0.13 m with the radius of curvature of 0.14 m, and it contained 256 piezoelectric transmitting elements and eight receiving elements. The 256 transmitting elements were divided equally to eight sectors so that each sector contained 32 transmitting elements and one receiving element on the edge. The geometry of the transducer is presented schematically in Fig. 2.5.

A more in-depth view of the data acquisition chain is presented in Fig. 3.4. A computer was controlling the generator cabinet which was generating the 10-cycle ultrasound pulses with desired amplitude, frequency and timing according to the designed sonication protocol. These pulses produced by the generator cabinet were forwarded to the transducer which used clusters formed from one, three and 32 transmitting elements to produce the desired sinusoidal pulses.

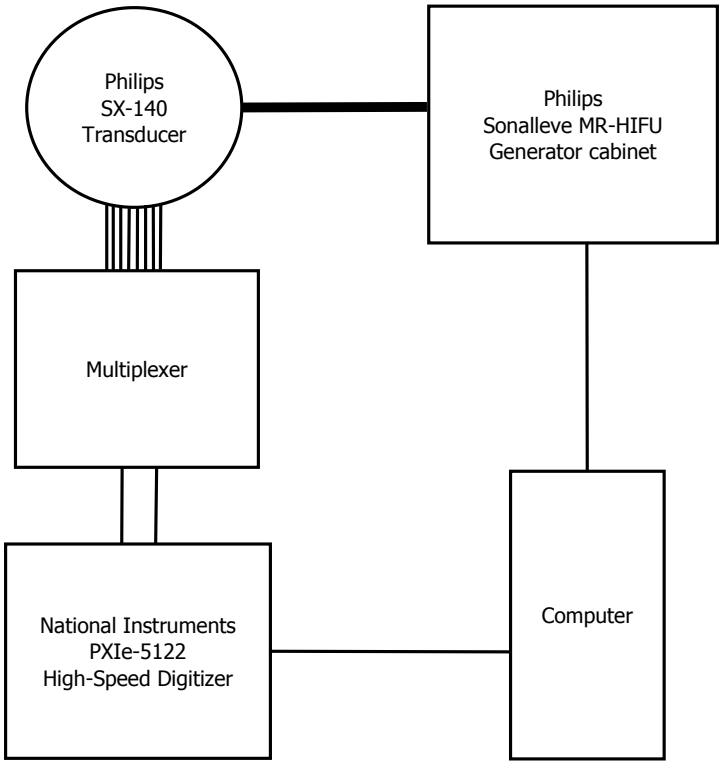

Figure 3.4: Schematic presentation of the data acquisition chain. Computer was controlling the generator cabinet which tranmitted 10-cycle ultrasound pulses for the predetermined transducer TX channels according to the sonication protocol. The eight RX channels were connected to NI PXIe-5122 High-Speed Digitizer via 8-to-2 channel multiplexer and finally to the computer for data acquisition.

The pulses were sent subsequently from each of the eight sectors one at a time and the reflections from the sonication target (i.e pin or pork meat) were acquired with all the eight receiving elements using the multiplexer to switch between them. These reflections were sampled at 100 MHz rate by high-speed digitizer (National Instruments, PXIe-5122) and finally saved by the computer for further data analysis. Hence, in total $8 \times 8 = 64$ reflections were acquired per sonication.

Because the desire was to track movement, two sonications were performed as described above in order to calculate the shift. The first one in the reference position i.e. the focus point of the transducer and the second one in the shifted position. The exact amount and direction of the shift were known because of the use of the three-axis motor drive.

3.2.1 Multiplexer design

All the other measurement equipment except for the multiplexer were commercially available products. The need for multiplexer rose because the hight-speed digitizer had only two channels for the data acquisition while in total eight receiving channels were used in the transducer during the measurements. This means that the channels should have been switched manually, which would have been both laborious and slow. Hence, the eight transducer channels had to be forwarded to those two channels available in the high-speed digitizer using the multiplexer between them as presented in Fig. 3.4.

The design for the multiplexer was similar to Analog Devices 4-to-1 multiplexer ADG659 which is presented in Fig. 3.5. The multiplexer was made using two parallel

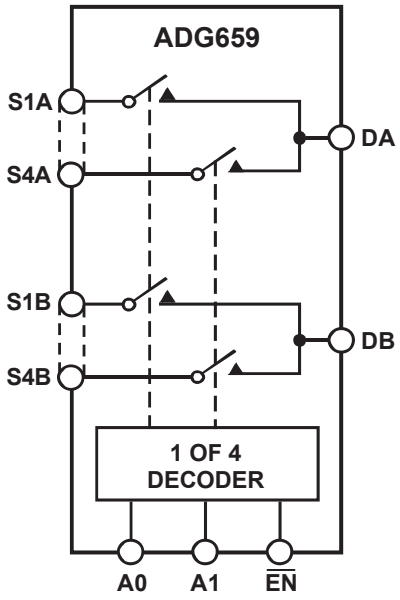

Figure 3.5: Schematic presentation of the implemented Analog Devices 4-to-1 ADG659 multiplexer circuit design. [52]

ADG659 integrated circuit components. The multiplexer switched two of its eight inputs in S1A – S4A and S1B – S4B to common outputs DA and DB, respectively. The input channels were controlled by 2-bit binary address lines A0 and A1. By applying different combinations of +5 V and 0 V voltages at different timings to these binary address lines, the input channel could be changed simultaneously for DA and DB drains. For example, applying 0 V to both address lines A0 and A1 switches the input channels S1A and S1B to the drains DA and DB, respectively. The $\overline{\text{EN}}$ input can be used to enable or disable the device but it was not needed in the experiment. The applied voltage was produced by a programmable USB device (National Instruments, DAQ M Series USB-6210).

The receiving transducers channels 1, 3, 5 and 7 were connected to the inputs S1A – S4A of the first circuit and the channels 2, 4, 6 and 8 to the same inputs in the second circuit. This allowed to acquire reflections simultaneously with two acquisition channels which means that four pulses had to be sent subsequently from each transmitting cluster in order to record the reflections with all the receiving channels. The channels S1B – S4B in both circuits were unused.

3.2.2 Software

LabVIEW (National Instruments) graphical programming language was used to design the user interface and controls for the high-speed digitizer (National Instruments, PXIe-5122) and the programmable USB device (National Instruments, DAQ M Series USB-6210) whereas to create the displacement calculation algorithms used in the data analysis.

3.3 Simulations of the acoustic fields

The simulations of the acoustic fields produced by the transmitting element clusters used in this experiment have been made according to the theory presented in reference [53]. The acoustic field emitted by a transducer or element cluster depends on its geometry i.e. the number, arrangement and orientation of single elements. Thus, it is necessary to know the field resulting from a single element in order to calculate the total acoustic field. To calculate the field of a single element, we use Rayleigh integral which gives the pressure field for given normal velocities on an infinite plane. We assume the acoustic medium to be linear, non-attenuating and homogeneous.

The Rayleigh integral is defined as [54]:

$$P(x,y,z) = 2\pi \frac{\rho\, u\, \nu}{\lambda} \iint_S \frac{\exp(i\vec{k}\cdot\vec{r})}{\vec{k}\cdot\vec{r}}\, dS \tag{3.24}$$

where P is the full sound pressure at point (x,y,z), ρ is the density of acoustic medium, S is the surface area of the element, ν is the frequency of the emitted ultrasound pulse and u is the velocity of the element surface which is usually the same as the particle velocity. The wave vector $\vec{k}$ is expressed as:

$$\|\vec{k}\| = \frac{2\pi}{\lambda} \tag{3.25}$$

where λ is the ultrasound wavelength. The orientation of the vector $\vec{k}$ is defined by the direction of propagating ultrasound wave. The vector $\vec{r}$ goes from the infinitesimal surface integration point dS to the Cartesian calculation point (x, y, z) as presented in Fig. 3.6. The modulus and the orientation of the vector $\vec{r}$ are

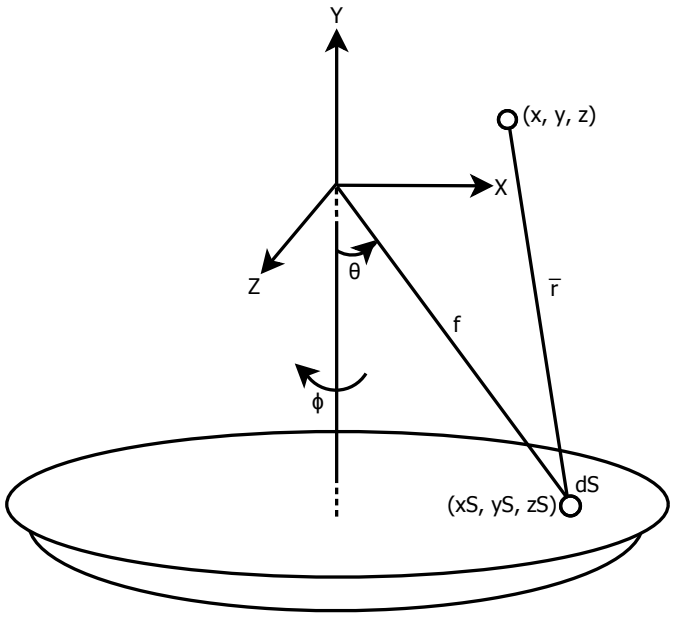

Figure 3.6: The spherical coordinate frame used to integrate the acoustic field on the surface of the transducer.

hence obtained by calculating the distance between the integrated surface element $(x_\mathrm{S}, y_\mathrm{S}, z_\mathrm{S})$ and the point where the sound pressure is calculated (x, y, z):

$$\vec{r} = (x - x_\mathrm{S})\hat{i} + (y - y_\mathrm{S})\hat{j} + (z - z_\mathrm{S})\hat{k} \tag{3.26}$$

$$\|\vec{r}\| = \sqrt{(x - x_\mathrm{S})^2 + (y - y_\mathrm{S})^2 + (z - z_\mathrm{S})^2}\ . \tag{3.27}$$

If the orientation of the propagating ultrasound wave is parallel to vector $\vec{r}$, the denominator in Eq. (3.24) simplifies to form:

$$\vec{k} \cdot \vec{r} = \|\vec{k}\|\|\vec{r}\|\ . \tag{3.28}$$

The integral of the sound field is on the emitting surface S of the transducer which in our case has spherical shape. Thus it is desirable to use the spherical coordinate system (θ, φ, f) to express the coordinates of the single element $(x_\mathrm{S}, y_\mathrm{S}, z_\mathrm{S})$ and the infinitesimal surface point dS. The transition from Cartesian to spherical coordinates is defined by the following relations:

$$x_\mathrm{S} = f \sin\theta \cos\varphi \tag{3.29}$$

$$y_\mathrm{S} = -f \cos\theta \tag{3.30}$$

$$z_\mathrm{S} = f \sin\theta \sin\varphi \tag{3.31}$$

$$dS = f^2 \sin\theta\, d\theta\, d\varphi\ . \tag{3.32}$$

However, as the transducer is symmetrical about the x-axis (the vertical direction), it is enough to calculate only the half-plane $z = 0$ and $x > 0$ of the acoustic field. All the other points in space can be derived by the formula:

$$P(x, y, z) = P(\sqrt{x^2 + z^2}, y, 0) \ . \tag{3.33}$$

Thus, the calculation of the acoustic field of a single element in all-space summarizes in equation:

$$P(x, y, 0) = 2\pi \frac{\rho\, u\, \nu}{\lambda} 2f^2 \int_{\theta=0}^{\theta_{\max}} \int_{\varphi=0}^{\pi} \frac{\exp(i\vec{k} \cdot \vec{r})}{\vec{k} \cdot \vec{r}} \sin\theta \, d\varphi \, d\theta \tag{3.34}$$

where

$$\vec{k} \cdot \vec{r} = \frac{2\pi}{\lambda} \sqrt{x^2 + y^2 + f^2 + 2f(y\cos\theta - x\sin\theta\cos\varphi)} \tag{3.35}$$

This Rayleigh equation yields a complex number whose modulus and argument represent the amplitude and phase of the oscillating wave, respectively.

The variable θ is defined from 0 to $\theta_{\max}$ which the opening angle of the single element. The variable φ varies from 0 to 2π but as the function is an odd function depending on the variable φ, it is preferable to integrate only from 0 to π and then multiply the result by 2. This simplification allows halving the number of grid points in integration. The developed expression for $\vec{k} \cdot \vec{r}$ in Eq. (3.35) also speeds up the computing speed by a factor of 2 because the number of terms in sine and cosine is less. [53]

We have now introduced tools to calculate the acoustic field produced by a single element. However, in our experiments, the element clusters were formed from one, three and 32 individual elements. Because all these elements are identical, it is possible to obtain the acoustic field produced by these clusters by a simple rotation and summation process introduced next.

First we have to calculate the field produced by a single element located in the center of the transducer. The sound pressure field emitted by our single element with the radius of 3.3 mm and the radius of curvature of 140.0 mm calculated with Eq. (3.34) is shown in Fig. 3.7. Because the radius of the curvature is large compared to the element diameter, the acoustic field produced by a single element diverges rather than focuses in the focal point of the transducer as seen in the figure.

In order to calculate the acoustic field emitted by the actual elements located in the edge of the transducer rather than in the center, we have to use rotation matrix:

$$\begin{aligned}
\begin{bmatrix} X \\ Y \\ Z \end{bmatrix} &= \begin{bmatrix} \cos\theta_n & \sin\theta_n & 0 \\ -\sin\theta_n & \cos\theta_n & 0 \\ 0 & 0 & 1 \end{bmatrix} \times \begin{bmatrix} \cos\varphi_n & 0 & \sin\varphi_n \\ 0 & 1 & 0 \\ -\sin\varphi_n & 0 & \cos\varphi_n \end{bmatrix} \times \begin{bmatrix} x \\ y \\ z \end{bmatrix} \\
&= \begin{bmatrix} \cos\theta_n\cos\varphi_n & \sin\theta_n & \cos\theta_n\sin\varphi_n \\ -\sin\theta_n\cos\varphi_n & \cos\theta_n & -\sin\theta_n\sin\varphi_n \\ -\sin\varphi_n & 0 & \cos\varphi_n \end{bmatrix} \times \begin{bmatrix} x \\ y \\ z \end{bmatrix}
\end{aligned} \tag{3.36}$$

where angles θ_n and φ_n correspond to the angular position of the center of the nth element in the spherical coordinate system. The pressure value present at the rotated

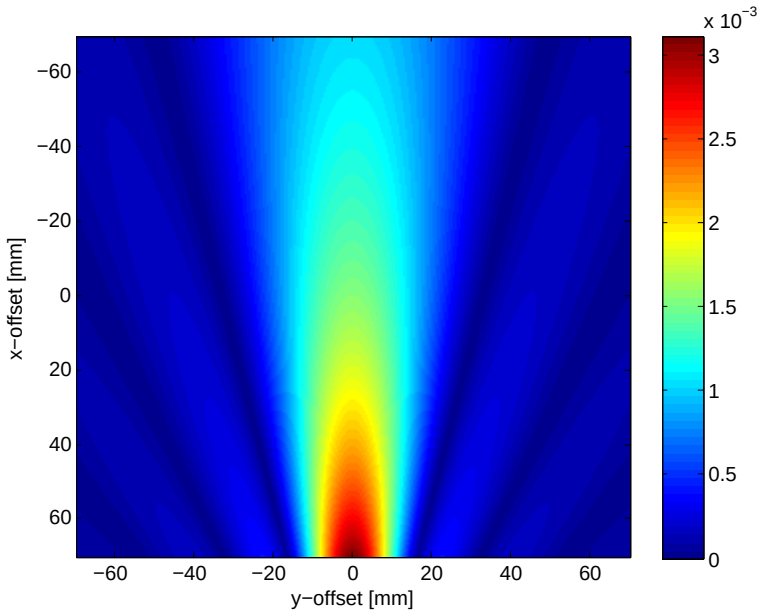

Figure 3.7: Acoustic field produced by a single element with a diameter of 6.6 mm, 14 cm radius of curvature and 1.20 MHz operating frequency located in the centre of the transducer.

coordinates (X, Y, Z) thus corresponds to the one present at location (x, y, z) of the original center element. Furthermore, this rotation operation has to be calculated for each point (x, y, z) of the space. The width of the rotated window is smaller by factor $\sqrt{2}$ because the diagonal shall not exceed the width of the initial window.

Because the ultrasound field is presented in an array form of pressure values, the rotation to a certain angle forces us to use linear interpolation to calculate the pressure value at a specific point in the array. Linear interpolation imposed by the rotation introduces rounding of calculations. Thus, it is desirable to calculate the initial center element field in Fig. 3.7 with sufficient enough resolution in order to avoid the rounding of these pressure values.

If the pressure field varies little spatially, the acoustic pressure oscillates with a spatial period $\lambda = 1$ mm. A size of at least 0.05 mm between each point is required to rebuild each of the wave oscillation from 20 points per period. Because of the rotational symmetry of the element centred, only the points in the plane $z = 0$ and $x > 0$ are necessary. In this way the real and imaginary part of the sound pressure generated by an element centred in a half plane 70 mm wide with a resolution of 0.05 mm can be stored in memory of 31 MB with floating point numbers. [53] After the rotation of the acoustic fields produced by each desired element, the rotated fields are summed together in space to obtain the total acoustic field in three dimensions.

3.4 Error estimation

The error estimates for the measurement results were calculated using the root-mean-square error (RMSE) formula:

$$\mathrm{RMSE} = \sqrt{\frac{\sum_{i=1}^{N}(\hat{\theta}_i - \theta_i)^2}{N}} \tag{3.37}$$

where θ_i is the observed value for the ith observation, $\hat{\theta}_i$ is the predicted value and N is the number of observations. In our case we are comparing the actual displacement with the estimated (predicted) displacement. RMSE is a frequently used measure of the differences between values predicted by a model or an estimator and the values actually observed. For normally distributed measurement points one can expect 68% of the θ_i values to be within one RMS error, and 95% to be within two RMS errors of the predicted values [55].

4 Results and discussion

4.1 Simulations of the acoustic fields

The method introduced in section 3.3 allows calculating the acoustic field of an element cluster or a transducer consisting of identical single elements. It assumes the acoustic medium i.e. the ultrasound path to be linear, non-attenuating and homogeneous. These assumptions are realistic in water whose attenuation for ultrasound at HIFU frequencies is very small (0.0022 dB/cm/MHz at 1 MHz [16]) and it can be thought to act as vibrating unit particles.

The simulated acoustic fields of the element clusters used in the actual experiment are presented in Fig. 4.1. These fields are calculated using the Rayleigh

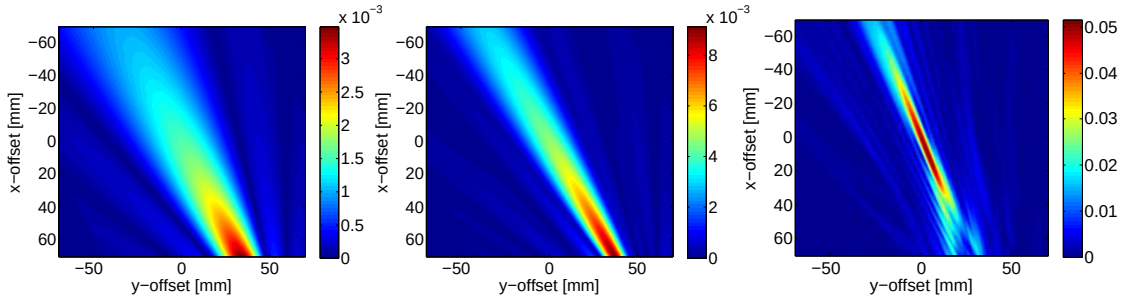

(a) (b) (c)

Figure 4.1: Simulated ultrasound fields using (a) one, (b) three and (c) 32 transmitting elements.

integral in Eq. (3.34) together with the rotation matrix in Eq. (3.36) derived in the previous section. The geometrical focus (which is also the focal point of the transducer) is located at coordinates (0, 0) in the figures. The pressure scales are in arbitrary units but they are comparable to each other.

Fig. 4.1(a) presents part of the acoustic field produced by a single element located on the edge of the transducer. The beam emitted by one transmitting element is wide close to the transducer surface and its pressure drops rapidly when approaching towards the focal point. This is because the radius of curvature i.e. θ-term in Eq. (3.34) is not remarkable with small element clusters and hence the focusing effect is not clearly visible.

The situation is a little different when looking at Fig. 4.1(b) presenting the acoustic field produced by an element cluster consisting of three transmitting elements. This element cluster is located in the same place as in the previous case but the beam axis is now narrower and its pressure is stronger close to the focal point. This is because the spherical shape of the transducer i.e. the focusing effect becomes stronger with large number of elements and hence the beam diverges less than with single transmitting element.

In Fig. 4.1(c) is seen the acoustic field produced by an element cluster consisting of 32 transmitting elements. In this case the orientation of the beam axis (the angle) is no longer the same as it was with one or three transmitting elements because the

elements are now distributed evenly from the bottom of the transducer to the edge rather than only on the edge. The difference in the beam axis orientation causes an error in the displacement calculations which assume the transmitting elements to be located only on the edge of the transducer. This assumption is true with one and three transmitting elements but the condition does not hold in the case of 32 elements. Indeed, the deviation of the displacement estimates is highly related to the orientation of the beam axis as we will see in the next section.

The error in the orientation can be corrected however by defining the coordinates of the transmitting element cluster to be somewhere halfway between the edge and the center of the transducer. This however, is always an approximation since we do not know the exact orientation of the beam axis the way we knew it with one and three transmitting elements where the exact coordinates of those elements could be used.

The beam axis in Fig. 4.1(c) is also very narrow when compared to the previous cases. The width of the beam axis can be thought as the "field of view" of the element cluster. If the beam axis is very narrow, it means that its pressure drops rapidly when moving little aside from it. This also reduces the amplitude of the reflection obtained from a target located at this very same point. The small amplitude of the reflection correspondingly might cause an error in the cross-correlation calculation of that particular element cluster, which in turn leads to a miscalculated displacement estimate.

4.2 Verification measurements

The aim of the verification measurements was to test the two different motion-tracking algorithms introduced in the sections 3.1.1 and 3.1.2 and also to determine their accuracy in target displacement estimation. A metal pin with ball-shaped end (diameter approximately 3 mm) was used as the sonication target in this experiment. This target was chosen because the reflections obtained from it has the sinusoidal shape (see Fig. 4.2) which improves the performance of cross-correlation algorithm in finding the correct time-shift value t_i. The numerical displacement estimates

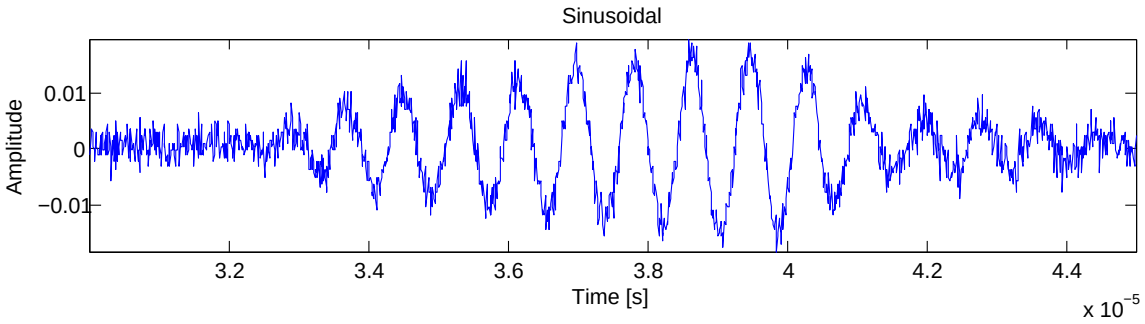

Figure 4.2: The signal reflected from the metal pin scatterer has the original sinusoidal pattern of the transmitted signal, which improves the performance of the cross-correlation algorithm.

calculated with both methods are presented in appendices A – C for element clusters consisting of one, three and 32 elements, respectively.

The correlation of the calculated estimates with the actual displacements in x-axis is presented in Fig. 4.3. The displacement data was acquired in the range from

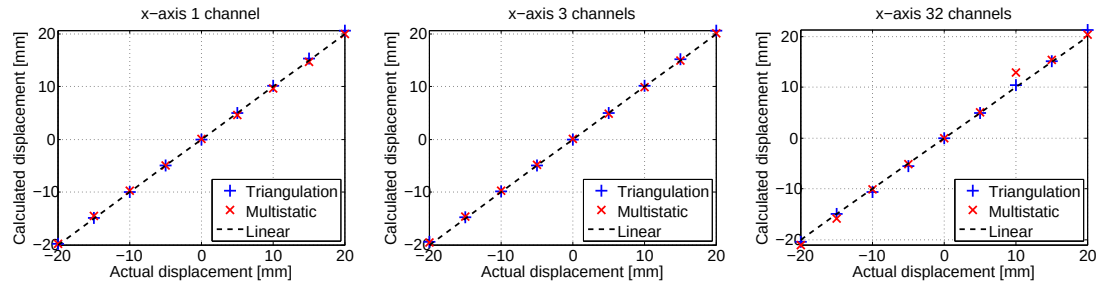

Figure 4.3: Correlation of the calculation estimates with respect to the actual shift in x-axis using (a) one, (b) three and (c) 32 transmitting elements.

–20 mm to 20 mm for x-axis with 5 mm step size. The coordinates are presented in MRI coordinate frame, which in Sonalleve MR-HIFU means that the x-axis is parallel to the ultrasound beam axis of the transducer.

The reflections received from the pin scatterer had the 10-cycle sinusoidal pattern of the transmitted pulses and hence the cross-correlation yielded the correct time shift t_i in most cases. Fig. 4.3(a) and Fig. 4.3(b) show that the calculated estimates along x-axis follow the actual displacement (dashed line) accurately with both calculation methods when using one or three transmitting elements. There is practically no difference in the estimation performance between one and three elements in this case.

However, the displacement estimates show more variation when 32 transmitting elements are used as seen in Fig. 4.3(c). This is partly due to the stated fact that the orientation of the beam axis for this transmitting element cluster is not the same as in the case of one or three elements. The difference in the orientation is clearly seen in simulations when comparing Fig. 4.1(b) and Fig. 4.1(c) for example. The beam axis for the latter case is more vertical when compared to one and three elements.

The different orientation of the beam axis results in an error in the triangulation displacement estimate which assumes the orientation to be according to Eq. (3.2) where the elements $i \in \{1...8\}$ are located on the edge of the transducer. Similarly, in the case of multistatic method the transmitting element $i = \mathrm{T}$ in Eq. (3.9) is assumed to be located on the edge. Thus, in the case of 32 elements the vertical angle of the beam axis differs so much from the assumed one that it causes an error in the calculated displacement estimates.

Another issue that affects the accuracy of the displacement estimates in triangulation method is the orientation of the displacement vector $\vec{d}$ i.e. the direction of the displacement with respect to the ultrasound beam axis. If the displacement vector is normal with respect to the beam axis of an element cluster, it induces a

fast decorrelation of the reflection and the axial displacement becomes more difficult to estimate accurately [7].

It has been shown that the correlation of the estimates with the actual displacement reaches its maximum when the displacement vector $\vec{d}$ is parallel to the beam axis. Correspondingly, the minimum correlation of the displacement estimates with actual shift occurs when the the beam axis is perpendicular to the displacement. Furthermore, the value of the correlation depends on the ratio between the displacement amplitude and the size of the ultrasound focus point. [7] Hence, for a given perpendicular displacement, a smaller element cluster yields better displacement estimates due to the larger ultrasound focus point.

In our experiments eight element clusters were used in triangulation displacement estimation. Hence, it is highly probable that when moving along three-dimensional space, the beam axes of some element clusters are parallel to the displacement and correspondingly some other are perpendicular to the displacement. The use of multiple element clusters thus helps to yield correct displacement estimates regardless of the direction of the movement.

The angles between the beam axis of each element cluster also affect the accuracy of the displacement estimates. To ensure the maximum accuracy of the displacement estimation, the angles between the beam axes should be maximized for each element cluster [56]. This means that the more close the element clusters are located to the edge of the transducer the better they perform in estimating the three-dimensional displacement. In the case of 32 elements, the beam axes are located more close to the centre than with one and three elements and hence the estimation accuracy is also reduced.

In conclusion, to maximise the correlation of the estimates with the actual displacement in every direction, the element clusters have to be chosen so that the ultrasound focus point is large enough when compared to the amplitude of the displacement. Moreover, by using small element clusters i.e. one or three elements, their relative distance can be increased, which improves the robustness of the estimates. [7, 56, 57]

All in all, the displacement estimates along x-axis are rather accurate also because the transducer focal point has an ellipsoidal shape which is longer in that direction (size approximately $1 \times 1 \times 7$ mm^3 [21]). Maybe more interesting is to observe the calculation accuracy along y- and z-axes in which directions the ellipsoidal shape is narrower. Because the reference estimate is in the centre of the focal point, it is predictable that when we approach to the edge of this ellipsoidal focal point, the accuracy of the calculated estimate will decrease. The y- and z-axes are ultrasonically symmetric because of the spherical shape of the transducer, and hence the accuracy of the estimates along these two axes should correspond to each other.

The displacement estimates calculated in y-axis are presented in Fig. 4.4. The displacement data was acquired in the range from –25 mm to 25 mm for y-axis with 5 mm displacements. More variation in the accuracy of the calculated estimates is observed here when comparing to the estimates along x-axis. When looking at the results with one transmitting element in Fig. 4.4(a), the displacement estimates correlate nicely with the actual shift in the range from –20 mm to 15 mm with tri-

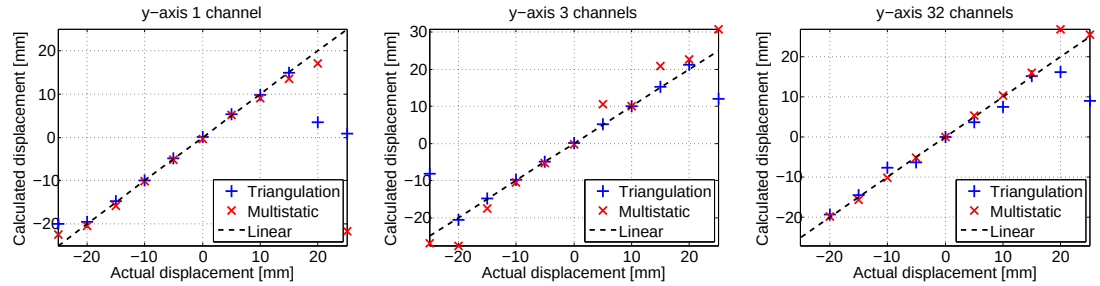

(a) (b) (c)

Figure 4.4: Correlation of the calculation estimates with respect to the actual shift in y-axis using (a) one, (b) three and (c) 32 transmitting elements.

angulation method and from –20 mm to 20 mm with multistatic method. However, beyond these two ranges both the triangulation and the multistatic calculations yield results which do not follow the actual shift. At –25 mm the estimates are still quite close to the actual shift with triangulation and multistatic methods (–19.91 mm and –22.43 mm, respectively) but at 25 mm both calculation results are completely arbitrary.

The reason for the failure of the calculated estimates in the extreme regions is that the backscattered signal gets weaker when moving towards the edge of the ultrasound focus point. This means that it is even harder to separate the actual reflection from the background noise both visually and in terms of cross-correlation. Therefore, when the reflected pulse is lost in noise, the cross-correlation yields abstract values for the time shift t_i, which in turn results in wrong displacement estimate.

Only one miscalculated t_i is enough to fail the obtained estimate, although in total we are using multiple t_is to calculate the results. Hence, it would be beneficial to somehow ignore the miscalculated t_is by observing the peak count or the amplitude value of cross-correlation results for each element cluster. This method was manually employed in the *in vitro* experiments (section 4.3) where the acquired speckles were even harder to separate from the background noise and other artefacts present in the signal.

In order to improve the estimation accuracy in the edge regions of the focus point, it would be desirable either to increase the amplitude of the reflected pulses by increasing the transmitting power or by using several transmitting elements instead. However, the drawback in the latter approach is that the beam axis gets narrower as the number of transmitting elements increases as seen in Fig. 4.1. As mentioned earlier, the narrow beam axis gives low amplitude reflection when the target is located at the edges. Displacement estimates of the larger element clusters also correlate worse with the actual displacement when the movement is perpendicular to the ultrasound beam axis [7].

The results obtained by keeping the power per element constant but using three and 32 transmitting elements instead of one are presented in Fig. 4.4(b) and Fig. 4.4(c), respectively. When looking at the calculated values along y-axis in Fig. 4.4(b), the multistatic method is able to find an estimate close to the actual shift

at –25 mm yielding –26.84 mm. At the same y-axis point the triangulation fails to give an accurate estimate due to the miscalculated t_is in the cross-correlation result. Again, it is observable that with 32 channels the deviation of the calculated estimates is greater compared to one and three elements. As mentioned, this is partly due to the different orientation of the beam axis and partly due to its narrower width.

There are also two miscalculated multistatic points visible in Fig. 4.4(b) at 5 mm and 15 mm locations where the multistatic method has estimated the shifts to be 10.47 mm and 20.85 mm, respectively. However, in the case of triangulation calculation the result is correct although the same measurement data was used in both cases. The multistatic method obtains the reflections transmitted by only one element compared to the triangulation method where each receiving element has its own transmitting element at the same location. Thus, some of the time shifts yielded by the cross-correlation have failed in the multistatic case, which resulted in the wrong estimates.

Calculated estimates along z-axis are presented in Fig. 4.5. Again, the displace-

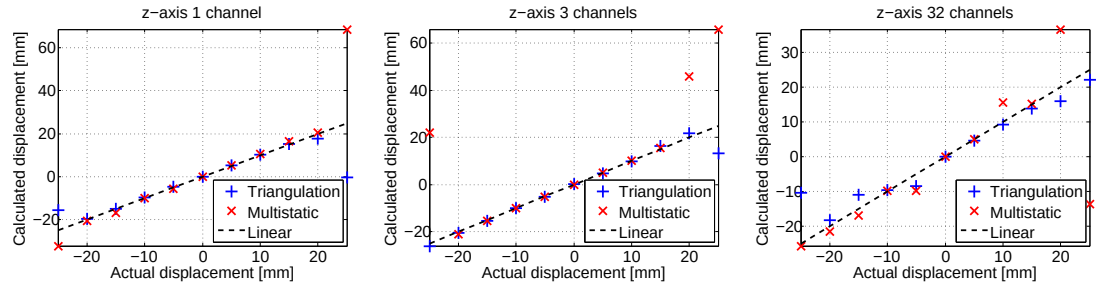

Figure 4.5: Correlation of the calculation estimates with respect to the actual shift in z-axis using (a) one, (b) three and (c) 32 transmitting elements.

ment data was acquired in the range from –25 mm to 25 mm for z-axis with 5 mm displacements. The results along z-axis should have the same accuracy as in the y-axis case because they are symmetric due to the spherical shape of the transducer.

Both calculation methods follow the actual shift in the range from –20 mm to 20 mm using only one transmitting channels as seen in Fig. 4.5(a). And as observed earlier, both methods fail to yield an accurate estimate beyond these two extremes. The results obtained with three transmitting elements in Fig. 4.5(b) correlate with the actual shift from –25 mm to 20 mm with the triangulation method and from –20 mm to 15 mm with the multistatic method. Beyond these regions, both methods fail to give an accurate estimate.

The triangulation method outperforms the multistatic method again in terms of the estimation range. Probably the reflections obtained from the same location as the ultrasound pulse was transmitted have slightly stronger amplitude (due to shorter travel distance) and hence the cross-correlation is able to find the correct time-shifts even near the edges of the focus point. In the case of 32 elements in Fig. 4.5(c), the deviation of the calculated estimates is again large and both methods are unable perform as well as with one and three elements. Hence, the size of the

element cluster [7] and the orientation of the beam axis has significant effect on the estimation accuracy in all three axes.

In addition to the one-dimensional displacement tracks along x-, y- and z-axes, the target was moved along three-dimensional path from location (–20, 20, –20) to (20, –20, 20) with $\sqrt{3} \times 5$ mm ≈ 8.66 mm displacement steps. The results obtained in the range from (–10, 10, –10) to (10, –10, 10) are presented in Fig. 4.6. Beyond this range the calculated estimates did not correlate with the actual displacements accurately and hence they are not presented here. However, the numerical values can be found from appendices A – C. The diameter of this range is $\sqrt{3} \times 20$ mm ≈ 34.64 mm which corresponds to the observed measurable range from –20 mm to 20 mm (40 mm) in the one-dimensional cases. Beyond this region, the amplitude of the backscattered signal is too weak to yield accurate estimates.

In Fig. 4.6(a) and Fig. 4.6(b) are presented the three-dimensional tracking curves with one and three transmitting elements, respectively. There is hardly no difference in terms of estimation accuracy when compared to one-dimensional cases presented earlier. The estimates follow the actual shift accurately in this range and both methods could also find the correct displacement at location (15, –15, 15) which is not presented here. The estimates with 32 elements are presented in Fig. 4.6(c) and again its performance is worse than in the latter cases due to the orientation of the beam axis. The multistatic method seems to perform a bit better than the triangulation but all in all the both methods yield estimates which do not correlate precisely with the actual shift in this case.

We can conclude that the range where the calculated estimates correspond to the real values is approximately 40 mm in width for one and three transmitting elements. This result is in accordance with the simulations, where the ultrasound beam width for one transmitting element (see Fig. 3.7) is approximately 35 mm. Also defining the correct orientation of the beam axis for each element cluster is significant factor affecting the estimation accuracy. The estimates obtained with 32 transmitting elements showed large deviation compared to one and three elements. This was because the orientation i.e. the vertical angle of the beam axis was different from the value of one and three elements.

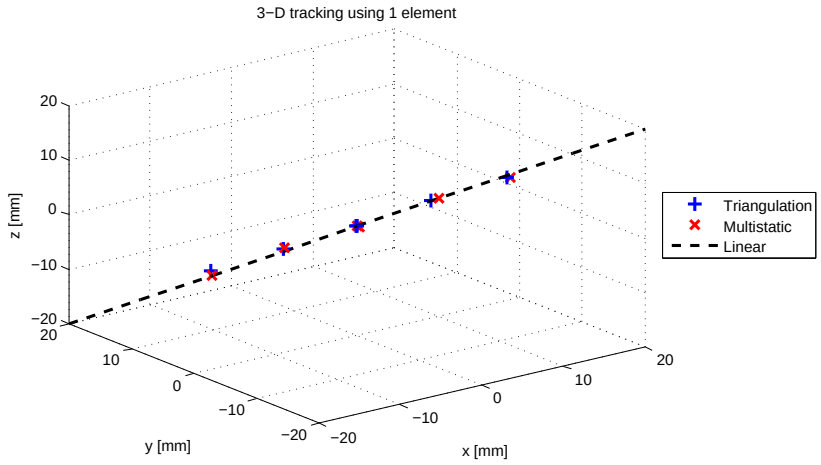

(a)

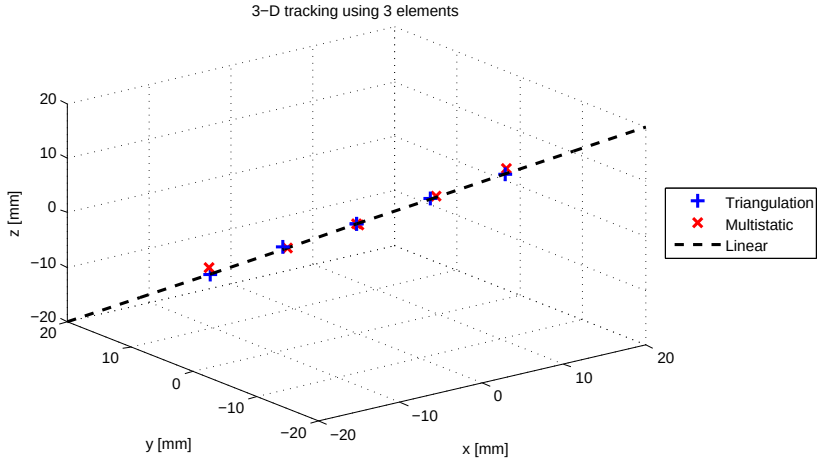

(b)

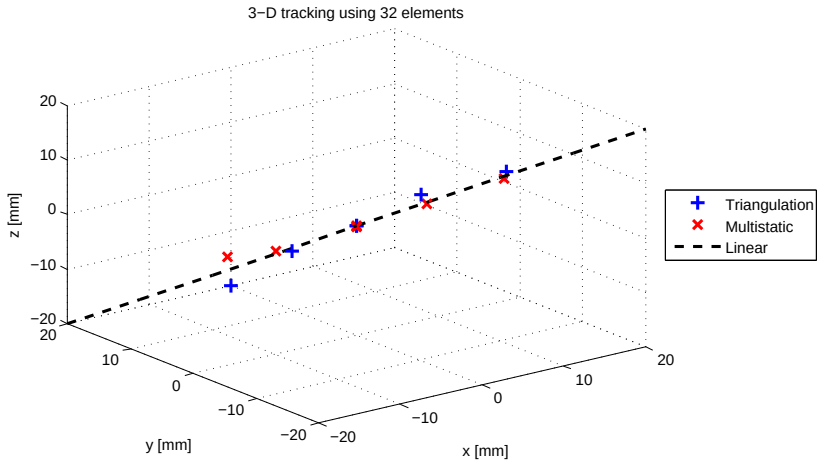

(c)

Figure 4.6: Correlation of the calculation estimates with respect to the actual shift in x-, y- and z-axis in the range from (–10, 10, –10) to (10, –10, 10) using (a) one, (b) three and (c) 32 elements.

4.3 In vitro experiments

The target used in *in vitro* experiments was a piece of pork meat with a size of 15 × 10 × 10 cm^3. The aim of this experiment was to mimic the movements of a liver in human body and thus validate the usefulness of the motion-tracking methods in the HIFU therapy for liver. The speckle received from the meat target has a random, although location specific pattern (see Fig. 4.7) which makes the motion-tracking possible. Thus, it differs from the sinusoidal pattern of the reflection received from

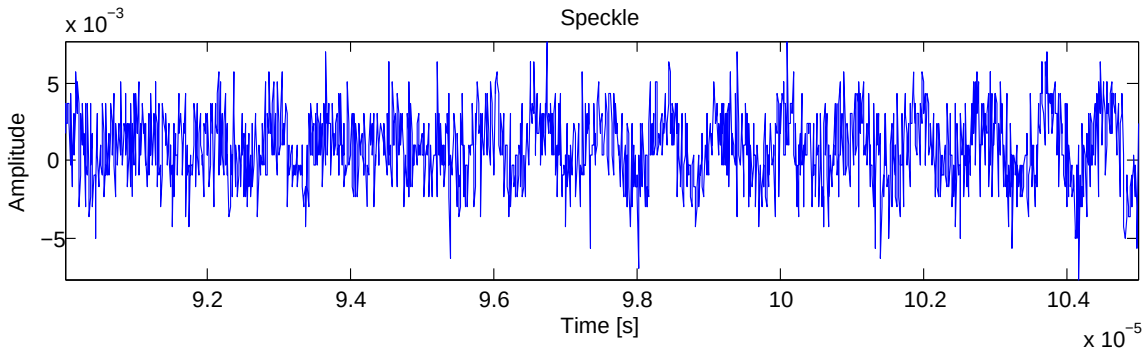

Figure 4.7: The speckle reflected from the meat scatterer has a random shape which is specific to the location from where it was reflected. The location specifity makes the motion-tracking possible.

the metal pin. The sinusoidal reflection is a lot easier to track in most cases because the cross-correlation algorithm is able to separate it from the background noise. The situation is somewhat different in speckle tracking where the cross-correlation algorithm sometimes cannot make difference with the speckle and the noise both of which have a random pattern. Also the speckles received from different parts of the meat can have similar shape, which leads to miscalculated time shifts.

An example of a failed cross-correlation result together with a successful one is presented in Fig. 4.8. In the failed one (see Fig. 4.8(a)) multiple peaks are present in the cross-correlation result and thus finding the correct one fails. The algorithm detects the time shift t_i from the peak with maximum amplitude value, which in this case would be approximately at sample index 1.8 × 10^4. This is however the wrong one because there might be other similar reflections (speckles) present in the received signal or the amplitude of the speckle is just simply too weak and hence lost in the background noise.

In the successful cross-correlation result (see Fig. 4.8(b)), the peak corresponding to the correct time shift is clearly visible at sample index 4.4 × 10^4. Now the amplitude of the correct peak is clearly higher than than the other peaks present in the signal and hence finding the correct time shift value is not a problem. Again, the other peaks are due to the other reflections which have a pattern shape close to the tracked speckle.

The problem with other speckles disturbing the cross-correlation algorithm can be reduced by windowing i.e. using a sampling window width where only the tracked

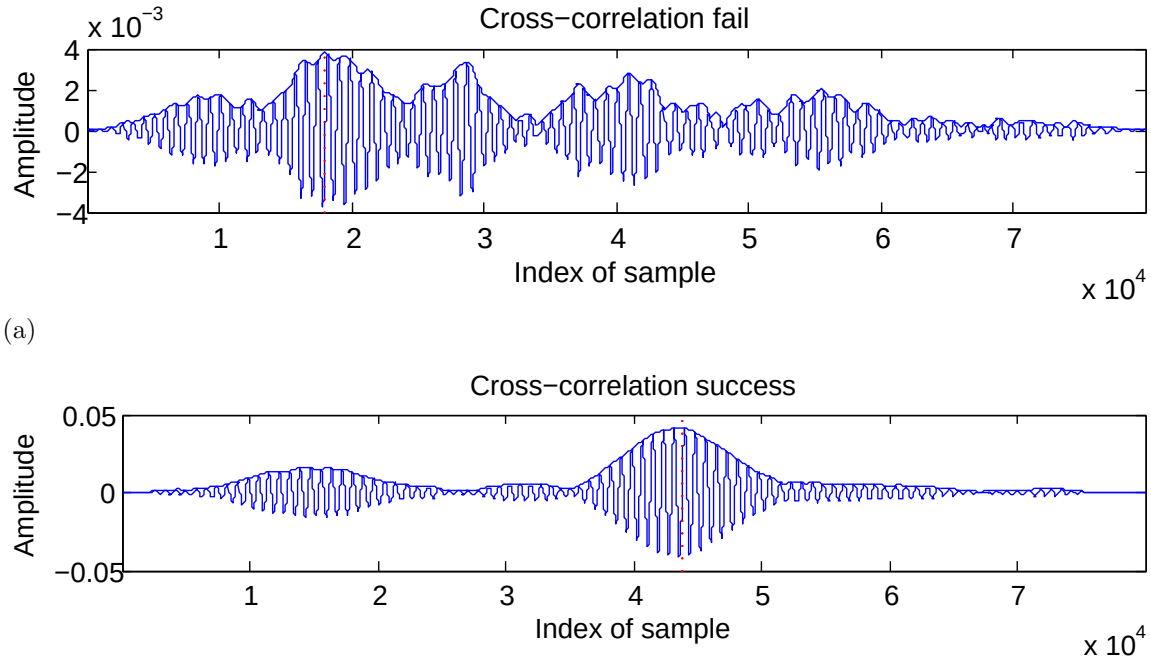

(a)

(b)

Figure 4.8: (a) The cross-correlation algorithm could not yield the correct time shift value due to the other higher amplitude peaks present in the outcome. (b) The cross-correlation algorithm is able to find the correct time shift value form the curve.

speckle is present. This however always requires a priori knowledge to estimate the location of the speckle in the sampling window. In order to improve the accuracy of the displacement estimates, optimal windowing widths were used for each position. Also using shorter pulse lengths would improve the measurement accuracy because the speckle or part of it would not move outside the sampling window so quickly. However, it was not possible to use shorter than 10-cycle pulses with the measurement system.

Before examining the results from the *in vitro* experiments, it has to be stated that a priori information was used also to exclude the elements where the speckle was not found. This was done manually by excluding the failed channels from the calculation algorithm. Although multiple failed channels were excluded in most cases, it was still possible to yield the correct three-dimensional calculation result as long as three channels were still available. In total seven and eight elements were available in multistatic and triangulation method, respectively.

An another issue which differs from the verification measurements is that only the triangulation algorithm was tested in this experiment. The reason for this was that the use of a priori information was only possible to employ in timely manner in this case. The failed channels were chosen by visually observing the time differences t_i and the results which were not in accordance with the actual displacement were excluded from the calculation. This was rather easy task in triangulation method

where the reflections were received in the same location as the pulse was transmitted. However, in the multistatic case, where one reflection was received with multiple elements located around the transducer, the choice of false t_is was more difficult to do by visually observing the time shifts.

The results from the triangulation speckle tracking in x-axis are presented in Fig. 4.9. The range in which the displacement data was acquired was from –5

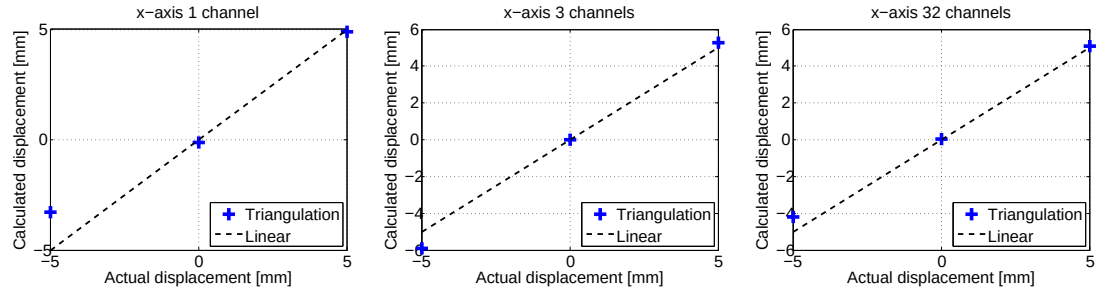

Figure 4.9: Correlation of the calculation estimates with respect to the actual shift in x-axis using (a) one, (b) three and (c) 32 transmitting elements.

mm to 5 mm with 5 mm step size. The smaller range compared to the verification measurements was due to the problems in finding the correct speckle in the signal and also because movement of a liver in x-axis direction is rather small: the liver moves approximately 20 mm in a breathing cycle [7] and this movement is mainly in feet-head direction in a human body, which in Sonalleve MR-HIFU corresponds to z-axis direction.

Motion-tracking along x-axis correlates well with the actual shift as long as the failed cross-correlation results are excluded from the calculation. In Fig. 4.9(a) and Fig. 4.9(b) the estimates are calculated using one and three transmitting elements, respectively. In these cases the orientation of the beam axis is correct and hence the triangulation algorithm is able yield results close to the actual shift after excluding the bad channels. In Fig. 4.9(c), presenting the displacement estimates with 32 transmitting channels, the obtained estimates also come close to the real values.

However, the estimates calculated in speckle tracking are not as accurate as in the verification experiment. The obtained time shifts might still not be exactly correct because the peak corresponding to the correct time shift is not smooth (see Fig. 4.8). This makes it harder to separate the correct one automatically from the multiple peaks and hence there might be variation also inside the correct peak, which causes an error in the estimate.

In Fig. 4.10 is presented the correlation of the calculated estimates with the actual shifts in the range from –10 mm to 10 mm again with 5 mm step size. The width of this range corresponds to the movement of a liver in human body which is reported to be 20 mm at maximum [7]. In Fig. 4.10(a) and Fig. 4.10(b) are shown the estimates with one and three transmitting elements, respectively. As stated earlier, there exists more variation in the accuracy than in the verification

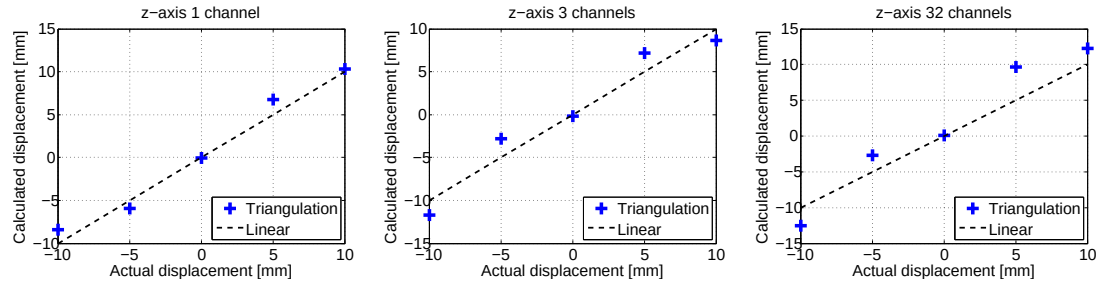

(a) (b) (c)

Figure 4.10: Correlation of the calculation estimates with respect to the actual shift in z-axis using (a) one, (b) three and (c) 32 transmitting elements.

measurements but the estimates still vary only ±2.20 mm at maximum compared to the actual shift. In Fig. 4.10(c) which presents the correlation with 32 elements, the variation is little greater at 5 mm yielding 9.68 mm.

From the *in vitro* experiments can be concluded that the speckle tracking is a lot harder to do than tracking a sinusoidal pulse. Multiple channels had to be manually excluded from the calculation in order to yield a displacement estimate close to the actual shift. Even after excluding the failed channels, the accuracy of speckle tracking was lower than that of the verification measurements due to the shape of the cross-correlation curve. Multiple peaks present in the curve resulted in the wrong time shift values which in turn yielded inaccurate displacement estimates. In practical applications, the selection of calculation channels should be done automatically by observing the peak count of cross-correlation curves or alternatively by determining a threshold value for the amplitude of the cross-correlation curve. The manual selection of the bad channels is a laborious task and could not be done in clinical applications.

4.4 Comparison of triangulation and multistatic radar motion-tracking techniques

The main difference between triangulation and multistatic motion-tracking methods is that the triangulation uses multiple transmitting and receiving element pairs which are physically near to each other. On the contrary, the multistatic method uses only one transmitting element and multiple receiving elements which are located around the transducer.

The choice which one is better depends mainly on the application the motion-tracking is desired to use for. If there exists an obstacle in the way of ultrasonic pulses in the some directions, the number of available elements might be limited. In HIFU liver application the obstacles preventing the penetration of ultrasound beam are usually rib bones which strongly reflect ultrasound beams due to the great difference in the acoustic impedance compared to the soft tissues [17]. The efficacy and accuracy of such systems is hence decreased when trying to treat a tumour located behind these obstacles, and it also prevents motion-tracking with elements

whose ultrasound beam intersects with the bone. Hence, it would be desirable to use only one transmitting element whose ultrasound path to the liver is available i.e. the multistatic method. In our design the reflections were received with seven elements in total and at least three of these have to be available to receive the reflection from the target.

However, the problem observed in the case of speckle tracking with multistatic method has to be solved. Now the selection of failed channels was difficult to do by visually inspecting the time delays and hence this process would have to be automated in the algorithm. This is also the case with triangulation method although the visual inspection of the time delays was easier. This could be made for example by observing the peak count in the cross-correlation curve or by defining an amplitude threshold for the cross-correlation peak corresponding to the correct time delay. This way the failed channels could be automatically excluded from the calculation algorithms.

The number of elements used in the element cluster is also a factor affecting the estimation accuracy. A larger number of transmitting elements results in a narrower ultrasound beam but on the other the reflection received from the target is also stronger. The large number of elements is also more inaccurate in observing motion perpendicular to the ultrasound beam axis in the triangulation method [7].

In order to track the target accurately the orientation of the beam axis also has to be approximated when multiple elements are employed. With one and three transmitting elements the accuracy of the displacement estimates was better for both of the tracking methods because the angle of the beam axis for each element cluster was known precisely. Also the angles of the beam axes were larger with one and three elements, which ensures the maximum accuracy of the displacement estimates [56].

The displacement estimation accuracies calculated using the root-mean-square error formula in Eq. (3.37) are shown in Tbl. 4.1 for each axis and element cluster. The errors were calculated from the same range as the displacement data was ac-

Table 4.1: Root-mean-square errors of the displacement estimates.

Number of elements	**Triangulation [mm]**			**Multistatic [mm]**		
	x	y	z	x	y	z
1	0.26	0.24	0.25	0.28	0.73	0.91
3	0.34	0.45	0.64	0.35	0.34	0.43
32	0.57	0.80	0.60	0.53	0.52	0.83

quired but using only the estimates whose residual to the actual shift was ± 2 mm at maximum i.e. the estimates which differed for more than 2 mm from the actual shift were excluded.

The accuracies with one and three transmitting elements are almost the same for both methods although there is a little less variation when using only one element.

Also one channel y- and z-axis errors are noticeable higher for multistatic method than one would expect. This is due to the couple miscalculated point located at 15 mm in Fig. 4.4(a) and at –15 mm in Fig. 4.5(a).

Using 32 transmitting elements yields larger errors than the latter cases in all three axes. As stated before, the angles of the beam axes for each element cluster were approximated to be the same as for one and three elements, which is not correct. This in turn results in larger deviation of the displacement estimates and is hence visible in the root-mean-square errors as well.

In Fig. 4.4(b) were also visible two displacement estimates at 5 mm and 15 mm locations, which were miscalculated by the multistatic method. However, the triangulation method could yield the correct displacements in the same locations. The sampling window in the multistatic case might contain reflections from a location which is not visible in the data acquired by the triangulation method. This in turn makes the cross-correlation algorithm to yield incorrect time shift value.

5 Conclusions

Two different ultrasound based techniques were introduced for the three-dimensional motion-tracking in HIFU therapy. The accuracies of these methods were determined and compared to each other. In addition, the results were analysed extensively together with the simulations of the acoustic fields. The speckle tracking capabilities of the triangulation method were also examined with *in vitro* experiments using a tissue mimicking liver.

The results from the verification experiments showed that the motion-tracking using the receiving elements of a spherical transducer is possible with both the triangulation and the multistatic methods. The displacement estimation accuracies of these two methods did not differ significantly, and therefore, the most suitable method should be selected depending on the accessibility of the tracked target.

The accuracy of the displacement estimation was mainly dependent on the size of the element cluster and the orientation of the beam axis. Using smaller number of transmitting elements and defining the orientation of the ultrasound beam axis for each element cluster accurately yielded more accurate estimates. The displacement estimates using the element cluster consisting of 32 transmitting elements had lower accuracy mainly because of these reasons.

The speckle tracking using the *in vitro* tissue sample was significantly more difficult to achieve than the motion-tracking using an ideal scatterer. First, the speckle had to be manually searched from the acquired signal by defining the sampling window length correctly, and secondly, if the speckle was not found in the signal, these channels had to be manually excluded form the calculation. This was both laborious and time consuming and hence could not be used during the HIFU therapy. This process could possibly be automated by observing the peak count and the amplitude of the cross-correlation curves.

Also the effect of pulse length on the estimation accuracy was not analysed. With shorter pulses the speckle tracking could have been more successful and yield more robust displacement estimates. It might have worked also without manually excluding the false time shifts. However, these issues were not investigated in this thesis, which leaves the field open for further research.

References

[1] M. O. Köhler, C. Mougenot, B. Quesson, J. Enholm, B. Le Bail, C. Laurent, C. T. W. Moonen, and G. J. Ehnholm. Volumetric HIFU ablation under 3D guidance of rapid MRI thermometry. *Medical Physics*, 36:3521, 2009.

[2] G. ter Haar, D. Sinnett, and I. Rivens. High intensity focused ultrasound-a surgical technique for the treatment of discrete liver tumours. *Physics in Medicine and Biology*, 34(11):1743, 1989.

[3] J. Y. Chapelon, J. Margonari, F. Vernier, F. Gorry, R. Ecochard, and A. Gelet. In vivo effects of high-intensity ultrasound on prostatic adenocarcinoma dunning r3327. *Cancer Research*, 52(22):6353 – 6357, 1992.

[4] F. Wu, Z. B. Wang, Y. D. Cao, W. Z. Chen, J. Z. Zou, J. Bai, H. Zhu, K. Q. Li, C. B. Jin, F. L. Xie, H. B. Su, and G. W. Gao. Changes in biologic characteristics of breast cancer treated with high-intensity focused ultrasound. *Ultrasound in Medicine & Biology*, 29(10):1487 – 1492, 2003.

[5] X. Fan and K. Hynynen. Ultrasound surgery using multiple sonications-treatment time considerations. *Ultrasound in Medicine & Biology*, 22(4):471 – 482, 1996.

[6] C. Damianou and K. Hynynen. Focal spacing and near-field heating during pulsed high temperature ultrasound therapy. *Ultrasound in Medicine & Biology*, 19(9):777 – 787, 1993.

[7] M. Pernot, M. Tanter, and M. Fink. 3-d real-time motion correction in high-intensity focused ultrasound therapy. *Ultrasound in Medicine & Biology*, 30(9):1239 – 1249, 2004.

[8] S. C. Davies, A. L. Hill, R. B. Holmes, M. Halliwell, and P. C. Jackson. Ultrasound quantitation of respiratory organ motion in the upper abdomen. *British Journal of Radiology*, 67(803):1096 – 1102, 1994.

[9] S. K. Ho and G. R. Chalmers. Instantaneous 3-d target location resolution utilizing only bistatic range measurement in a multistatic system. Patent, April 2007. US 7205930.

[10] NDT Resource Center. Introduction to ultrasonic testing. `http://www.ndt-ed.org/index_flash.htm`, July 2012.

[11] H. Kuttruff. *Ultrasonics fundamentals and applications*. Elsevier Applied Science, 1991.

[12] Uni Basel Department of Physics. Diffraction at ultrasonic waves. `http://physik.unibas.ch/Praktikum/VPII/PDF/acousto_optic.pdf`, July 2012.

[13] T. Yano, M. Tone, and A. Fukumoto. Range finding and surface characterization using high-frequency air transducers. *Ultrasonics, Ferroelectrics and Frequency Control, IEEE Transactions on*, 34(2):232 – 236, March 1987.

[14] J. E. Kennedy, G. R. ter Haar, and D. Cranston. High intensity focused ultrasound: surgery of the future? *British Journal of Radiology*, 76(909):590 – 599, 2003.

[15] G. D. Ludwig. The Velocity of Sound through Tissues and the Acoustic Impedance of Tissues. *Acoustical Society of America Journal*, 22:862, 1950.

[16] R. S. C. Cobbold. *Foundations of Biomedical Ultrasound*. Biomedical Engineering Series. Oxford University Press, 2007.

[17] K. K. Shung. *Diagnostic Ultrasound: Imaging and Blood Flow Measurements*. Taylor&Francis, 2006.

[18] J. Baun. Physical principles of general and vascular sonography. `http://www.jimbaun.com/2_interaction_softtissue.pdf`, July 2012.

[19] University of Connecticut Department of Physics. Constructive and destructive interference. `http://www.phys.uconn.edu/~gibson/Notes/Section5_2/Sec5_2.htm`, July 2012.

[20] National Physical Laboratory. Speed of sound in gases and vapours. `http://www.kayelaby.npl.co.uk/general_physics/2_4/2_4_1.html`, July 2012.

[21] M. Köhler. *Sonication methods and motion compensation for magnetic resonance guided high-intensity focused ultrasound*. PhD thesis, Helsinki University of Technology, 2009.

[22] M. Pernot, J. F. Aubry, M. Tanter, J. L. Thomas, and M. Fink. High power transcranial beam steering for ultrasonic brain therapy. *Physics in Medicine and Biology*, 48(16):2577, 2003.

[23] L. R. Gavrilov and J. W. Hand. A theoretical assessment of the relative performance of spherical phased arrays for ultrasound surgery. *Ultrasonics, Ferroelectrics and Frequency Control, IEEE Transactions on*, 47(1):125 – 139, January 2000.

[24] D. R. Daum and K. Hynynen. A 256-element ultrasonic phased array system for the treatment of large volumes of deep seated tissue. *Ultrasonics, Ferroelectrics and Frequency Control, IEEE Transactions on*, 46(5):1254 – 1268, September 1999.

[25] B. D. de Senneville, C. Mougenot, and C. T. W. Moonen. Real-time adaptive methods for treatment of mobile organs by mri-controlled high-intensity focused ultrasound. *Magnetic Resonance in Medicine*, 57(2):319 – 330, 2007.

[26] E. W. Wood and A. L. Loomis. Xxxviii. the physical and biological effects of high-frequency sound-waves of great intensity. *Philosophical Magazine Series 7*, 4(22):417 – 436, 1927.

[27] W. J. Fry. Production of focal destructive lesions in the central nervous system with ultrasound. *Journal of Neurosurgery*, 11:471 – 478, 1954.

[28] W. J. Fry, F. J. Fry, J. W. Barnard, R. F. Krumins, and J. F. Brennan. Ultrasonic lesions in the mammalian central nervous system. *Science*, 122(3168):517 – 518, 1955.

[29] H. E. Cline, J. F. Schenck, K. Hynynen, R. D. Watkins, S. P. Souza, and F. A. Jolesz. Mr-guided focused ultrasound surgery. *Journal Of Computer Assisted Tomography*, 16(6):956 – 965, 1992.

[30] H. E. Cline, K. Hynynen, C. J. Hardy, R. D. Watkins, J. F. Schenck, and F. A. Jolesz. Mr temperature mapping of focused ultrasound surgery. *Magnetic Resonance in Medicine*, 31(6):628 – 636, 1994.

[31] Y. Ishihara, A. Calderon, H. Watanabe, K. Okamoto, Y. Suzuki, K. Kuroda, and Y. Suzuki. A precise and fast temperature mapping using water proton chemical shift. *Magnetic Resonance in Medicine*, 34(6):814–823, 1995.

[32] S. D. Nandlall, E. Jackson, and C. C. Coussios. Real-time passive acoustic monitoring of hifu-induced tissue damage. *Ultrasound in Medicine & Biology*, 37(6):922 – 934, 2011.

[33] C. C. Coussios, C. H. Farny, G. Ter Haar, and R. A. Roy. Role of acoustic cavitation in the delivery and monitoring of cancer treatment by high-intensity focused ultrasound (hifu). *International Journal of Hyperthermia*, 23(2):105 – 120, 2007.

[34] M. Gyöngy, M. Arora, A. Noble, and C. C. Coussios. A passive array technique for cavitation mapping during hifu treatment. *The Journal of the Acoustical Society of America*, 123(5):3223 – 3223, 2008.

[35] J. C. Hindman. Proton resonance shift of water in the gas and liquid states. *The Journal of Chemical Physics*, 44(12):4582 – 4592, 1966.

[36] F. Bloch. Nuclear Induction. *Physical Review*, 70:460 – 474, October 1946.

[37] J. Poorter. Noninvasive mri thermometry with the proton resonance frequency method: Study of susceptibility effects. *Magnetic Resonance in Medicine*, 34(3):359 – 367, 1995.

[38] C. R. Hill, J. C. Bamber, and G. R. Haar. *Physical Principles of Medical Ultrasonics*. John Wiley & Sons, 2005.

[39] S. A. Sapareto and W. C. Dewey. Thermal dose determination in cancer therapy. *International Journal of Radiation Oncology*Biology*Physics*, 10(6):787 – 800, 1984.

[40] N. J. McDannold, R. L. King, F. A. Jolesz, and K. H. Hynynen. Usefulness of mr imaging-derived thermometry and dosimetry in determining the threshold for tissue damage induced by thermal surgery in rabbits1. *Radiology*, 216(2):517 – 523, 2000.

[41] N. McDannold, K. Hynynen, D. Wolf, G. Wolf, and F. Jolesz. Mri evaluation of thermal ablation of tumors with focused ultrasound. *Journal of Magnetic Resonance Imaging*, 8(1):91 – 100, 1998.

[42] K. Hynynen, O. Pomeroy, D. N. Smith, P. E. Huber, N. J. McDannold, J. Kettenbach, J. Baum, S. Singer, and F. A. Jolesz. Mr imaging-guided focused ultrasound surgery of fibroadenomas in the breast: A feasibility study1. *Radiology*, 219(1):176 – 185, 2001.

[43] C. M. C. Tempany, E. A. Stewart, N. McDannold, B. J. Quade, F. A. Jolesz, and K. Hynynen. Mr imaging-guided focused ultrasound surgery of uterine leiomyomas: A feasibility study1. *Radiology*, 226(3):897 – 905, 2003.

[44] G. K. Hesley, J. P. Felmlee, J. B. Gebhart, K. T. Dunagan, K. R. Gorny, J. B. Kesler, K. R. Brandt, J. N. Glantz, and B. S. Gostout. Noninvasive treatment of uterine fibroids: Early mayo clinic experience with magnetic resonance imaging-guided focused ultrasound. *Mayo Clinic Proceedings*, 81(7):936 – 942, 2006.

[45] R. Chopra, L. Curiel, R. Staruch, L. Morrison, and K. Hynynen. An mri-compatible system for focused ultrasound experiments in small animal models. *Medical Physics*, 36(5):1867 – 1874, 2009.

[46] A. Schweikard, G. Glosser, M. Bodduluri, M. J. Murphy, and J. R. Adler. Robotic motion compensation for respiratory movement during radiosurgery. *Computer Aided Surgery*, 5(4):263 – 277, 2000.

[47] C. J. Ritchie, C. R. Crawford, J. D. Godwin, K. F. King, and K. Yongmin. Correction of computed tomography motion artifacts using pixel-specific back-projection. *Medical Imaging, IEEE Transactions on*, 15(3):333 – 342, June 1996.

[48] M. Tanter, M. Pernot, J. F. Aubry, G. Montaldo, F. Marquet, and M. Fink. Compensating for bone interfaces and respiratory motion in high-intensity focused ultrasound. *International Journal of Hyperthermia*, 23(2):141 – 151, 2007.

[49] M. Ries, B. D. de Senneville, S. Roujol, Y. Berber, B. Quesson, and C. Moonen. Real-time 3d target tracking in mri guided focused ultrasound ablations in moving tissues. *Magnetic Resonance in Medicine*, 64(6):1704 – 1712, 2010.

[50] H. D. Kubo and B. C. Hill. Respiration gated radiotherapy treatment: a technical study. *Physics in Medicine and Biology*, 41(1):83, 1996.

[51] M. Tillander. Pressure field measurements of a therapeutic ultrasound transducer. Master's thesis, Helsinki University of Technology, 2007.

[52] *Analog Devices 4- and 8-Channel Analog Multiplexers technical manual*.

[53] C. Mougenot. *L'asservissement par IRM d'un réseau matriciel ultrasonore et ses applications thérapeutiques*. PhD thesis, L'Université Bordeaux, 2005.

[54] F. Fahy. *Foundations of Engineering Acoustics*. Academic Press, 2001.

[55] Stanford University Department of Statistics. Rms error. `http://www-stat.stanford.edu/~susan/courses/s60/split/node60.html`, July 2012.

[56] M. Tanter, J. Bercoff, L. Sandrin, and M. Fink. Ultrafast compound imaging for 2-d motion vector estimation: application to transient elastography. *Ultrasonics, Ferroelectrics and Frequency Control, IEEE Transactions on*, 49(10):1363 – 1374, October 2002.

[57] L. Capineri, M. Scabia, and L. Masotti. A doppler system for dynamic vector velocity maps. *Ultrasound in Medicine & Biology*, 28(2):237 – 248, 2002.

A Displacement estimates with one element

Actual [mm]			**Triangulation [mm]**			**Multistatic [mm]**		
x	y	z	x	y	z	x	y	z
–20.0	0.0	0.0	–19.86	–0.14	0.55	–19.76	–0.99	–0.15
–15.0	0.0	0.0	–14.89	–0.15	0.39	–14.51	–0.41	0.92
–10.0	0.0	0.0	–9.97	0.02	0.41	–9.68	–0.74	–0.25
–5.0	0.0	0.0	–5.00	–0.10	0.26	–4.91	0.05	–0.21
0.0	0.0	0.0	0.02	0.11	0.07	0.10	–0.32	0.04
5.0	0.0	0.0	4.96	–0.07	–0.03	4.66	–0.39	–0.94
10.0	0.0	0.0	10.15	0.08	–0.43	9.67	0.18	–0.90
15.0	0.0	0.0	15.31	0.10	–0.15	14.72	–0.16	–0.82
20.0	0.0	0.0	20.67	–0.17	–0.40	20.01	0.22	–0.25
0.0	–25.0	0.0	0.69	–19.91	–2.20	–2.57	–22.43	–4.57
0.0	–20.0	0.0	1.13	–19.54	0.59	–0.39	–20.39	–0.92
0.0	–15.0	0.0	0.84	–14.80	0.50	–0.21	–15.87	0.33
0.0	–10.0	0.0	0.34	–9.90	–0.07	–0.41	–10.09	–0.72
0.0	–5.0	0.0	0.07	–4.88	0.07	0.00	–5.14	0.57
0.0	0.0	0.0	0.02	0.11	0.07	0.10	–0.32	0.04
0.0	5.0	0.0	0.18	5.37	0.26	0.10	5.14	–0.02
0.0	10.0	0.0	0.38	9.80	–0.06	0.72	9.03	0.57
0.0	15.0	0.0	0.99	14.94	–0.12	1.26	13.51	–0.35
0.0	20.0	0.0	–0.59	3.45	–6.71	–33.63	17.06	8.47
0.0	25.0	0.0	7.28	0.92	–12.27	7.56	–21.71	–11.01
0.0	0.0	–25.0	–2.73	–10.25	–15.64	–2.22	–15.24	–32.21
0.0	0.0	–20.0	1.06	–0.36	–19.51	–1.02	1.65	–20.44
0.0	0.0	–15.0	0.43	0.27	–14.80	–0.49	–0.60	–16.71
0.0	0.0	–10.0	0.15	0.10	–9.74	–0.18	0.10	–10.00
0.0	0.0	–5.0	0.00	–0.17	–4.73	–0.07	–0.68	–5.66
0.0	0.0	0.0	0.02	0.11	0.07	0.10	–0.32	0.04
0.0	0.0	5.0	0.32	0.06	5.16	0.29	0.03	5.42
0.0	0.0	10.0	0.74	–0.16	10.18	0.45	–0.03	10.54
0.0	0.0	15.0	1.24	0.31	15.10	0.21	0.15	16.60
0.0	0.0	20.0	–1.68	–16.58	17.83	1.92	–3.57	20.47
0.0	0.0	25.0	–13.93	–7.96	–0.38	–2.37	–32.96	68.58
–20.0	20.0	–20.0	–18.50	2.93	–12.55	–21.69	19.45	–56.28
–15.0	15.0	–15.0	–11.76	1.40	–27.01	11.11	–9.01	–39.81
–10.0	10.0	–10.0	–9.21	11.27	–10.02	–10.14	9.82	–9.88
–5.0	5.0	–5.0	–4.85	5.32	–4.81	–4.92	5.15	–4.64
0.0	0.0	0.0	0.02	0.11	0.07	0.10	–0.32	0.04
5.0	–5.0	5.0	5.46	–4.82	4.95	5.52	–5.91	5.85
10.0	–10.0	10.0	11.26	–9.42	9.43	10.55	–10.82	10.31
15.0	–15.0	15.0	15.64	–16.32	16.48	6.51	0.84	–10.61
20.0	–20.0	20.0	–2.55	–16.22	–0.52	9.69	–58.14	9.92

B Displacement estimates with three elements

Actual [mm]			Triangulation [mm]			Multistatic [mm]		
x	y	z	x	y	z	x	y	z
–20.0	0.0	0.0	–19.47	–0.25	1.66	–19.57	–0.94	–0.01
–15.0	0.0	0.0	–14.71	–0.33	0.73	–14.61	0.13	0.75
–10.0	0.0	0.0	–9.86	–0.07	0.46	–9.70	–0.28	0.34
–5.0	0.0	0.0	–4.91	0.07	0.33	–4.84	0.07	0.43
0.0	0.0	0.0	0.02	0.02	0.07	0.09	–0.29	0.01
5.0	0.0	0.0	5.07	0.11	0.00	4.91	0.10	0.13
10.0	0.0	0.0	10.23	0.06	–0.04	9.93	0.10	0.04
15.0	0.0	0.0	15.27	0.01	–0.08	14.91	0.02	–0.03
20.0	0.0	0.0	20.70	–0.10	–0.15	20.15	–0.03	0.37
0.0	–25.0	0.0	–2.70	–8.10	3.07	–0.85	–26.84	–1.43
0.0	–20.0	0.0	1.87	–20.66	0.29	2.62	–27.54	7.81
0.0	–15.0	0.0	0.94	–14.89	0.02	0.30	–17.50	0.77
0.0	–10.0	0.0	0.37	–9.79	0.72	–0.80	–10.49	0.33
0.0	–5.0	0.0	0.20	–5.00	0.22	0.10	–5.36	0.10
0.0	0.0	0.0	0.02	0.02	0.07	0.09	–0.29	0.01
0.0	5.0	0.0	0.03	5.06	0.65	–3.96	10.47	–5.02
0.0	10.0	0.0	0.58	10.00	0.15	0.31	9.97	0.09
0.0	15.0	0.0	0.95	15.21	1.87	–0.49	20.85	4.90
0.0	20.0	0.0	1.64	21.15	0.19	–0.31	22.55	0.72
0.0	25.0	0.0	–7.25	12.00	3.78	–31.84	30.81	–58.85
0.0	0.0	–25.0	1.46	–0.24	–26.04	–63.89	70.35	21.92
0.0	0.0	–20.0	1.07	0.39	–20.51	–0.13	1.06	–21.01
0.0	0.0	–15.0	0.45	0.05	–15.30	0.06	–0.27	–15.45
0.0	0.0	–10.0	0.28	–0.59	–9.89	0.04	–0.54	–10.11
0.0	0.0	–5.0	–0.01	–0.05	–5.09	–0.02	–0.19	–5.11
0.0	0.0	0.0	0.02	0.02	0.07	0.09	–0.29	0.01
0.0	0.0	5.0	0.20	0.18	4.83	0.06	–0.20	5.03
0.0	0.0	10.0	0.67	–0.31	9.94	0.22	–0.65	10.03
0.0	0.0	15.0	1.53	0.84	16.48	–0.01	0.04	15.50
0.0	0.0	20.0	2.40	1.13	21.67	2.63	2.63	45.83
0.0	0.0	25.0	–2.39	27.15	13.37	–8.37	24.00	65.86
–20.0	20.0	–20.0	–14.11	22.02	–6.66	NaN	NaN	NaN
–15.0	15.0	–15.0	–9.14	17.15	–31.70	–86.52	84.24	–51.70
–10.0	10.0	–10.0	–8.55	12.13	–11.70	–9.76	10.80	–9.50
–5.0	5.0	–5.0	–4.91	5.29	–4.84	–4.79	4.81	–4.91
0.0	0.0	0.0	0.02	0.02	0.07	0.09	–0.29	0.01
5.0	–5.0	5.0	5.57	–4.52	4.91	5.41	–5.55	5.85
10.0	–10.0	10.0	11.21	–9.16	9.46	10.36	–10.35	11.42
15.0	–15.0	15.0	15.65	–18.68	16.87	14.62	–16.07	15.97
20.0	–20.0	20.0	3.07	2.15	24.46	15.93	–60.81	–14.92

C Displacement estimates with 32 elements

Actual [mm]			**Triangulation [mm]**			**Multistatic [mm]**		
x	y	z	x	y	z	x	y	z
–20.0	0.0	0.0	–20.48	–0.75	–0.42	–21.02	1.07	–0.32
–15.0	0.0	0.0	–14.98	0.58	0.73	–15.90	0.62	0.15
–10.0	0.0	0.0	–10.59	–1.62	0.12	–10.12	0.04	0.55
–5.0	0.0	0.0	–5.50	–1.30	–0.27	–5.08	–0.01	0.16
0.0	0.0	0.0	0.01	0.01	0.01	–0.04	0.00	–0.05
5.0	0.0	0.0	5.01	0.29	0.03	5.12	–0.24	–0.07
10.0	0.0	0.0	10.48	–1.33	–1.59	12.96	–4.48	–8.47
15.0	0.0	0.0	15.16	–1.18	–0.23	15.39	–0.21	0.03
20.0	0.0	0.0	21.37	1.24	0.65	20.42	–0.62	–0.99
0.0	–25.0	0.0	1.52	–21.80	1.37	–0.05	–27.14	0.88
0.0	–20.0	0.0	0.93	–19.44	2.09	–0.18	–19.90	1.89
0.0	–15.0	0.0	0.85	–14.59	1.46	0.70	–15.68	0.76
0.0	–10.0	0.0	0.69	–7.70	0.92	0.79	–10.27	0.39
0.0	–5.0	0.0	–0.31	–6.32	0.03	–0.19	–5.18	0.48
0.0	0.0	0.0	0.01	0.01	0.01	–0.04	0.00	–0.05
0.0	5.0	0.0	–0.18	3.61	–0.41	–0.06	5.26	0.46
0.0	10.0	0.0	0.26	7.45	–0.47	–0.21	10.37	0.52
0.0	15.0	0.0	0.94	15.18	–0.86	–0.16	16.04	0.24
0.0	20.0	0.0	1.01	16.22	–2.41	–5.60	26.97	–4.33
0.0	25.0	0.0	–3.75	9.08	–11.30	0.88	25.61	2.73
0.0	0.0	–25.0	–2.98	6.02	–10.51	–3.70	2.60	–25.71
0.0	0.0	–20.0	0.75	–2.56	–18.31	–0.79	–0.53	–21.65
0.0	0.0	–15.0	1.78	0.94	–10.99	–2.91	1.61	–16.91
0.0	0.0	–10.0	–0.37	–2.29	–9.65	–0.68	0.82	–9.83
0.0	0.0	–5.0	1.32	1.73	–8.56	–2.51	1.45	–9.77
0.0	0.0	0.0	0.01	0.01	0.01	–0.04	0.00	–0.05
0.0	0.0	5.0	0.49	0.57	4.57	0.88	–0.59	4.95
0.0	0.0	10.0	1.03	1.84	9.12	1.62	–2.65	15.45
0.0	0.0	15.0	1.52	2.04	13.85	0.84	–0.07	15.12
0.0	0.0	20.0	1.96	0.66	15.93	1.97	6.43	36.58
0.0	0.0	25.0	–1.37	–12.43	22.11	19.91	10.26	–13.77
–20.0	20.0	–20.0	–7.23	22.93	–46.91	–7.14	–42.12	–51.36
–15.0	15.0	–15.0	–11.17	23.67	–29.89	NaN	NaN	NaN
–10.0	10.0	–10.0	–9.79	7.28	–10.84	–9.44	8.35	–6.05
–5.0	5.0	–5.0	–5.24	3.54	–4.43	–5.67	5.41	–4.93
0.0	0.0	0.0	0.01	0.01	0.01	–0.04	0.00	–0.05
5.0	–5.0	5.0	5.55	–2.99	5.15	4.62	–5.24	4.82
10.0	–10.0	10.0	11.78	–8.52	9.84	9.65	–10.93	10.45
15.0	–15.0	15.0	17.20	–13.32	12.37	15.66	–12.18	16.86
20.0	–20.0	20.0	7.18	–18.34	7.87	10.19	29.50	–17.27

D In vitro displacement estimates

Table D1: Displacement estimates with one transmitting element.

Actual [mm]			**Triangulation [mm]**		
x	y	z	x	y	z
–5.0	0.0	0.0	–3.27	2.03	2.14
0.0	0.0	0.0	–0.13	0.18	–0.05
5.0	0.0	0.0	4.89	–1.72	2.31
0.0	0.0	–10.0	–0.41	–5.58	–8.44
0.0	0.0	–5.0	–0.15	–2.18	–5.94
0.0	0.0	0.0	–0.13	0.18	–0.05
0.0	0.0	5.0	–0.25	–1.90	6.79
0.0	0.0	10.0	2.60	3.27	10.31

Table D2: Displacement estimates with three transmitting elements.

Actual [mm]			**Triangulation [mm]**		
x	y	z	x	y	z
–5.0	0.0	0.0	–5.90	–3.78	1.03
0.0	0.0	0.0	–0.01	0.23	–0.14
5.0	0.0	0.0	5.27	1.38	–1.26
0.0	0.0	–10.0	–1.94	5.08	–11.71
0.0	0.0	–5.0	0.56	–0.29	–2.84
0.0	0.0	0.0	–0.01	0.23	–0.14
0.0	0.0	5.0	2.02	3.35	7.20
0.0	0.0	10.0	0.88	–1.57	8.63

Table D3: Displacement estimates with 32 transmitting elements.

Actual [mm]			**Triangulation [mm]**		
x	y	z	x	y	z
–5.0	0.0	0.0	–4.18	–0.91	–1.39
0.0	0.0	0.0	0.05	–0.17	0.07
5.0	0.0	0.0	5.10	2.58	0.84
0.0	0.0	–10.0	4.38	–3.58	–12.58
0.0	0.0	–5.0	0.79	–2.44	–2.68
0.0	0.0	0.0	0.05	–0.17	0.07
0.0	0.0	5.0	1.74	2.55	9.68
0.0	0.0	10.0	–2.23	–6.29	12.23